Modeling urban traffic heat flux in the Community Earth System Model

Yuan Sun[1], Keith W. Oleson[2], Zhonghua Zheng[1]

[1]Department of Earth and Environmental Sciences, The University of Manchester, Manchester M13 9PL, UK
[2]Climate and Global Dynamics Laboratory, NSF National Center for Atmospheric Research, Boulder, CO 80307, USA

Key Points:

- We developed an urban traffic module in CESM to model traffic heat flux in a bottom-up way.
- Online traffic heat modeling improves the simulation of anthropogenic heat flux, which by default only accounts for building energy use.
- Traffic heat increased the simulated annual mean air temperature by 0.4 K and 0.25 K at FR-Capitole and UK-Manchester sites, respectively.

Corresponding author: Yuan Sun, yuan.sun@manchester.ac.uk

Corresponding author: Zhonghua Zheng, zhonghua.zheng@manchester.ac.uk

Abstract

Traffic is a major contributor to anthropogenic heat flux (AHF) in urban areas, amplifying urban heat island effects. However, few Earth system models explicitly represent traffic conditions and their associated heat emissions. This study introduces a new urban traffic module into the Community Earth System Model (CESM), enabling interactive simulation of traffic-related heat in urban areas. The module adopts a bottom-up approach to estimate traffic heat flux (Q_{traffic}) based on time-varying traffic flow and vehicle type distributions, while dynamically responding to meteorological conditions such as snow, rain, and low temperatures. Model validation was performed using observational data from two urban sites: Capitole of Toulouse, France (FR-Capitole), and Manchester, UK (UK-Manchester). At the FR-Capitole site, an annual mean Q_{traffic} of 22.23 W/m^2 in 2004 resulted in a simulated annual mean canopy air temperature increase of 0.4 °C, improving the simulated turbulent heat flux compared to observations. At the UK-Manchester site, the simulation with a yearly mean Q_{traffic} of 16.27 W/m^2 showed a 0.25 °C air temperature increase in 2022. These traffic-induced canopy warming also influenced the indoor environment, contributing to increased air conditioning use in summer and reduced building space heating demand in winter. This new functionality offers potential applications such as simulating traffic-induced AHF and its impacts on the climate system under future climate changes and energy transition scenarios.

Plain Language Summary

Urban traffic is a major source of anthropogenic heat, which can warm local thermal environments. However, most Earth system models (ESMs) do not include traffic-related anthropogenic heat in their simulations, so they fail to capture cities' real impact on the climate. In this study, we added a traffic module into the Community Earth System Model (CESM), an ESM that includes an urban climate model to explicitly represent and parameterize urban surface energy and water processes. The new module estimates traffic heat based on how traffic flow and vehicle heat emissions change over time, allowing this heat to directly affect the urban climate modeling. We tested the model at two urban sites: the Capitole of Toulouse, France (FR-Capitole), and Manchester, UK (UK-Manchester), and compared the results with real-world data. The annual average traffic heat flux (Q_{traffic}) was 22.23 W/m^2 at FR-Capitole, leading to a 0.4 °C increase in simulated air temperature in 2004. At UK-Manchester, incorporating a yearly mean Q_{traffic} of 16.27 W/m^2 raised the simulated air temperature by 0.25 °C in 2022. Our results show that traffic-induced temperature changes varied across cities, and they should be considered in urban climate modeling.

1 Introduction

Anthropogenic heat flux (AHF) influences the Earth system through thermal circulation and the transboundary transport of air pollutants (Tao et al., 2021; M. Xie et al., 2016). Urban areas, the primary source of anthropogenic heat emissions, face growing risks from extreme heat and deteriorating air quality (Ryu & Min, 2024). AHF amplifies urban heat island (UHI) effect (Shahmohamadi et al., 2011), accelerates near-surface O_3 formation (M. Xie et al., 2016), and increases uncertainty in atmospheric stability (N. Zhang et al., 2010). Accurately modeling AHF is therefore crucial for understanding and mitigating these impacts.

In urban areas, anthropogenic heat originates primarily from buildings, traffic, and human metabolism, with the relative contributions varying across regions and time. For example, in Greater London, UK, from 2005 to 2008, buildings accounted for 80% of total anthropogenic heat emissions, while traffic and human metabolism contributed 15% and 5%, respectively (Iamarino et al., 2012). In Beijing, China, however, traffic contributed 30% of total emissions, representing the second-largest source after the building sector

(45%), with industrial activities and human metabolism accounting for 20% and 5%, respectively (R. Sun et al., 2018). Two other cities in China, Chengdu and Chongqing, saw similar shares of anthropogenic heat emission in 2019 (Ming et al., 2022). In São Paulo, Brazil, traffic's share was even higher, reaching 50% (Ferreira et al., 2011). In some urban areas, such as Toulouse, France (Pigeon et al., 2007), Daegu, South Korea (Kim et al., 2022), traffic has emerged as the dominant source of AHF and a major contributor to the UHI effect in summer. Despite building space heating contributing significantly to AHF in winter, its influence diminishes in summer, when traffic becomes a relatively more dominant heat source. In addition, traffic increases road surface temperature. Chapman and Thornes (2005) reported a 1.5°C difference between inside and outside lanes of a busy UK motorway.

As AHF accounts for only about 1% of greenhouse gas forcing, global climate models initially neglected it in global climate simulations (Hertwig et al., 2021). However, since the 1970s, numerical models have incorporated anthropogenic heat to assess its climatic effects (Block et al., 2004; Washington, 1972). Flanner (2009) demonstrated that incorporating AHF in the Community Atmosphere Model (CAM) coupled with a slab ocean model warmed the substantial atmosphere up to 0.9°C under an AHF of 0.19 W/m^2, advocating its integration into global climate models (GCMs). Over the past decades, the use of GCMs and Earth system models (ESMs) for large-scale urban climate studies has been increasing (e.g., Fischer et al., 2012; McCarthy et al., 2012; Y. Sun et al., 2024; Yu et al., 2025; Zhao et al., 2021; Zheng et al., 2021). The Community Earth System Model (CESM) integrates a building energy model into its urban component, the Community Land Model Urban (CLMU), to simulate building-related AHF (Li, Zhao, Oleson, et al., 2024; Oleson & Feddema, 2020). However, considering only AHF from the building sector may lead to an underestimation of its impact on urban climate and the broader climate system.

In this study, we incorporate traffic heat flux into CESM and highlight two key advancements of our new traffic heat model. First, it incorporates multiple vehicle types, including conventional internal combustion engine vehicles (ICEVs), hybrid-electric vehicles (HEVs), and electric vehicles (EVs), allowing it to reflect the impacts of future transitions to cleaner energy sources. Second, it dynamically responds to varying weather conditions, such as cold spells, rainfall, and snowfall. These features enhance the model's potential for supporting future global urban climate adaptation efforts using CESM under changing climate and energy transition scenarios.

This paper is organized as follows: Section 2 presents a literature review for selecting a suitable approach for our model development. Section 3 describes the parameterization scheme, model validation method, and sensitivity analysis design. Section 4 shows simulation outputs in comparison with observations at two sites. Section 5 summarizes key findings of simulated traffic-induced thermal effects and discusses future directions of promoting the traffic module's application for larger scales.

2 Literature Review

We conducted a literature review in two parts. The first focuses on modeling techniques for integrating AHF within the GCMs/ESMs framework (Section 2.1), while the second focuses on traffic heat representation and parameterization in urban climate models (Section 2.2).

2.1 Integrating Anthropogenic Heat Flux in Global Climate Simulations

Early global climate simulations prescribed AHF as a constant to assess atmospheric model sensitivities, neglecting its spatial heterogeneity and temporal variations (e.g., Block et al., 2004; McCarthy et al., 2010; Washington, 1972). Flanner (2009) incorporated sea-

sonal and diurnal cycles as weighting factors to refine the spatial and temporal variability of AHF, improving upon the annual mean constant approach. G. J. Zhang et al. (2013) and B. Chen et al. (2014) applied more realistic estimations of global anthropogenic heat data based on present-day energy consumption into global simulations (Figure 1). AHF was estimated based on Sailor and Lu (2004)'s top-down approach, which converted large-scale statistical data (e.g., fuel consumption, population) into heat-emission flux. Recognizing the seasonal dependence of building energy use and the daily and hourly variations in travel behavior, detailed temporal profiles were applied for scaling heat emissions from buildings, traffic, and human metabolism (Sailor et al., 2015). This inventory-based approach, however, does not account for actual traffic conditions through in-situ observations. Moreover, transportation energy use may extend beyond urban traffic, such as highways, freight, or intercity travel, potentially leading to oversimplification or overestimation of urban traffic-related AHF. Relying on large-scale aggregated energy consumption statistics and reducing reliance on real-time local data, it is more suitable for prescribing AHF entering the atmosphere than influencing the land surface, as it omits the connection to the land surface, nor does it differentiate between urban and non-urban areas.

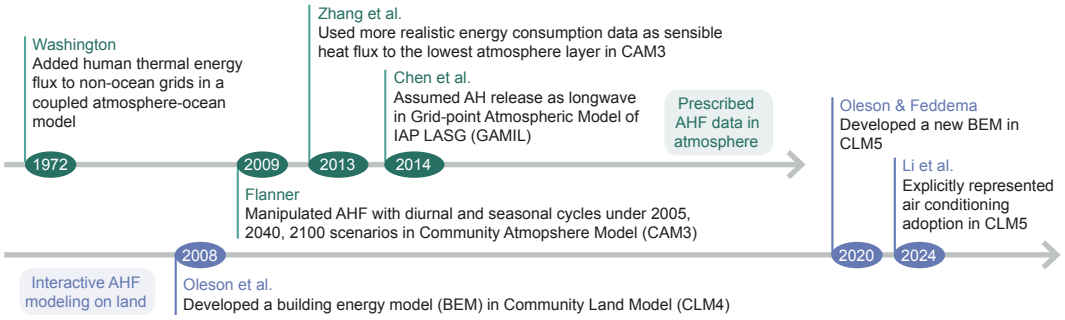

Figure 1. Timeline of incorporating anthropogenic heat in global climate simulation.

An alternative is to explicitly represent anthropogenic heat release processes in urban areas. This bottom-up approach aligns well with Earth system modeling, as it allows urban anthropogenic heat emissions to interact dynamically with local climate conditions. In the building sector, climate models integrated building energy modeling by calculating building-related heat flux based on indoor and outdoor air temperature (Bueno et al., 2012; F. Chen et al., 2011; Oleson et al., 2010). Advancements in building energy modeling within the GCMs/ESMs framework have enabled the online simulation of AHF from the building sector and the potential examination of AHF impacts on both the atmosphere and land (Li, Zhao, Qin, et al., 2024; Oleson & Feddema, 2020). In this context, vehicle-specific AHF is supposed to be quantified using bottom-up methods based on detailed traffic data (e.g., traffic volume, vehicle types, urban road types) (Smith et al., 2009).

2.2 Traffic-Related Anthropogenic Heat Flux in Urban Climate Models

Vehicle-specific AHF has not yet been integrated within ESMs, due to the lack of real-time traffic data and the limited representation and parameterization of urban surfaces at the global scale. Instead, multiple regional studies have incorporated AHF from vehicles into urban climate models using various approaches (Table 1). Some applied a top-down energy inventory-based estimation method (Equation C1), while others used bottom-up approaches relying on local vehicle data (Equation C2). The details of these

two methods were described in Appendix C. More complex process-based methods have also been developed, incorporating detailed parameterizations of vehicle-induced changes in radiation and wind, along with additional heat from tire friction to the road and exhaust emissions to the air (e.g., Xiao et al., 2018). However, they have not been widely adopted for urban climate models yet, considering spatial resolution, modeling complexity, and computational cost.

The Town Energy Balance (TEB) model initially incorporated traffic heat flux (Q_{traffic}) using a fixed annual average value of 8 W/m^2, scaled by a diurnal cycle, in a case study of Toulouse, France (Pigeon et al., 2008). This estimate was derived from surface energy balance measurements (Pigeon et al., 2007). Later, Khalifa et al. (2016) refined Q_{traffic} estimation in TEB using two approaches. One was explicit urban traffic representation, incorporating real-time urban traffic characteristics such as traffic volume, vehicle speed, and subsequent energy consumption to estimate sensible and latent heat fluxes. The other was process-based parameterization, accounting for not only turbulent heat fluxes but also radiation and momentum fluxes. This scheme incorporated detailed biogeophysical interactions with ambient conditions (e.g., radiation, temperature, wind). Such a process-based method involves complex parameterization and computational demands and has typically been applied at the microscale, relying on empirical studies of ICEVs (Fujimoto et al., 2012). In addition, Bohnenstengel et al. (2014) incorporated transport-movement profiles into the Met Office–Reading Urban Surface Exchange Scheme (MORUSES) to convert daily energy demand into vehicle-related AHF.

Traffic-induced thermal effects influence the simulations of temperature and heat fluxes in urban climate models. Ohashi et al. (2007) found overestimated near-surface air temperatures in an urban canopy model with a building energy analysis model (CM-BEM), due to their use of peak vehicle volume from in-situ observations to calculate automobile waste heat flux. Similarly, Chow et al. (2014) highlighted the significance of Q_{vehicle} in modeling AHF and its contribution to the UHI effect using the Weather Research & Forecasting Model (WRF) with a multi-layer urban scheme, the Building Effect Parameterization (BEP) and the Building Energy Model (BEM), i.e., WRF-BEP/BEM. In contrast, Juruš et al. (2016) found Q_{vehicle} to be insignificant in a large eddy simulation model, PALM, coupled with the Urban Surface Model (PALM-USM), where moderate traffic intensity resulted in minimal differences in simulations with or without traffic-related AHF.

Table 1. Estimating Traffic Heat Flux in Urban Climate Modeling.

Reference	Urban climate model	Urban climate scale	Method of traffic-related AHF	Traffic heat flux (Q_{vehicle})	Traffic-induced thermal effects	Follow-up studies (e.g.)
Ohashi et al. (2007)	CM-BEM	Local	Bottom-up estimation	Up to 100 W/m^2 (weekday) and 40 W/m^2 (holiday) in the evening hours of Kanda area, Tokyo, Japan	Overestimated near-surface air temperature by using the maximum traffic volume	Kikegawa et al. (2014); Takane et al. (2022)
Pigeon et al. (2008)	TEB	Local	Surface energy balance measurements	Annual average daily mean values of 8 W/m^2 in Toulouse, France, modulated by a diurnal cycle	Simulated AHF closer to inventory-based estimation	Bueno et al. (2011); Khalifa et al. (2016, 2018)
Bohnenstengel et al. (2014)	MORUSES	Meso	Top-down estimation	Annual average daily mean values of 2 W/m^2 in London, UK, modulated by a diurnal cycle	Smaller than the contribution of building-related AHF	None
Chow et al. (2014)	WRF-BEM+BEP	Meso	Bottom-up estimation	Diurnal varying (∼6–10 W/m^2) in Phoenix, US	Significance in quantifying AHF	F. Chen et al. (2016); B. Liu et al. (2021)
Juruš et al. (2016)	PALM-USM	Local	Bottom-up estimation	Diurnal varying (∼1–20 W/m^2) in Prague, Czech Republic	Insignificant changes in temperature and heat flux due to moderate traffic	Resler et al. (2017)

1 Climate scale classification is: 10–200 m (micro), 0.5–2 km (local), and 25–100 km (meso) (Oke et al., 2017).

Overall, previous studies have incorporated traffic heat flux in urban climate models through top-down, bottom-up, and physical-process-based approaches. To enable urban traffic heat modeling within the GCMs/ESMs framework, a bottom-up approach to accounting for traffic volume, vehicle type, number of lanes, and speeds is more realistic, as it offers greater specificity than conventional inventory-based methods. However, the complexity of traffic-related radiative and thermal processes should be simplified to maintain computational efficiency.

3 Method and Data

This study estimates traffic heat flux using a bottom-up approach that incorporates urban vehicle types, traffic volume, and road conditions. To balance computational demands, traffic-related fluxes are represented as a simplified field, Q_{traffic}, excluding explicit parameterization of detailed heat-generation processes such as tire friction, radiative heat, and exhaust heat from vehicles.

3.1 Modeling Urban Traffic Flux

3.1.1 Inserting Traffic Heat Flux into the Urban Surface Energy Balance

In CLMU, the default urban surface energy balance is (Equation 1):

$$\begin{aligned} R_{\text{n}} &= SW_{\text{down}} - SW_{\text{up}} + LW_{\text{down}} - LW_{\text{up}} \\ &= Q_{\text{h}} + Q_{\text{le}} + (Q_{\text{g}} - Q_{\text{ac}} + Q_{\text{heat}} - Q_{\text{v}}) - Q_{\text{heat}} - Q_{\text{w}} \\ &= Q_{\text{h}} + Q_{\text{le}} + Q_{\text{g}} - Q_{\text{ac}} - Q_{\text{v}} - Q_{\text{w}}, \end{aligned} \tag{1}$$

where R_{n} is net radiation on urban surfaces (W/m^2), calculated as the balance between upwelling and downward radiation fluxes. Specifically, SW_{up} and SW_{down} are upwelling and downward shortwave radiation fluxes. LW_{up} and LW_{down} are upwelling and downward longwave radiation fluxes. The net energy from R_{n} is then partitioned into ground heat flux and turbulent fluxes. Q_{h} is upward sensible heat flux, Q_{le} is upward latent heat flux, Q_{g} is urban heat flux into soil or snow, Q_{ac} is urban air conditioning flux, Q_{heat} is building space heating flux transferred from the indoor to the street canyon, Q_{w} is sensible heat flux from building space heating or cooling sources of urban waste heat, and Q_{v} is ventilation heat flux. Details on the CLMU are described in Oleson and Feddema (2020).

Q_{traffic} is traffic-induced heat flux, added to the surface energy balance as a distinct term, separate from the bulk sensible heat and latent fluxes (Equation 2):

$$\begin{aligned} R_{n} &= SW_{\text{down}} - SW_{\text{up}} + LW_{\text{down}} - LW_{\text{up}} \\ &= Q_{\text{h}} + Q_{\text{le}} + (Q_{\text{g}} - Q_{\text{ac}} + Q_{\text{heat}} - Q_{\text{v}}) - Q_{\text{heat}} - Q_{\text{w}} - Q_{\text{traffic}} \\ &= Q_{\text{h}} + Q_{\text{le}} + Q_{\text{g}} - Q_{\text{ac}} - Q_{\text{v}} - Q_{\text{w}} - Q_{\text{traffic}}. \end{aligned} \tag{2}$$

We do not explicitly partition traffic-induced heat into sensible heat and latent components in Equation 2 for two reasons. First, latent heat comprises only a small fraction of total traffic heat emissions. For ICEVs, reported values range from 6.6% (Teufel et al., 2021), 7.3% (Iamarino et al., 2012), 8% (Khalifa et al., 2018), to 10% (Afshari et al., 2018). For HEVs and EVs, the latent heat contribution is even smaller. Thus, we represent traffic heat as a single term, Q_{traffic}, for simplicity. Second, we treat Q_{traffic} in the same manner as building-related heat terms (i.e., Q_{ac}, Q_{heat}), which are separately included in the surface energy balance equation for downstream energy partitioning into turbulent fluxes (i.e., Q_{h}, Q_{le}). The model assumes the AHF coming into the climate system is from building energy consumption and urban traffic (Equation 3):

$$\text{AHF} = Q_{\text{heat}} + Q_{\text{w}} + Q_{\text{traffic}}, \tag{3}$$

where Q_{heat} represents traffic-related AHF and the sum of Q_{heat} and Q_{w} represents building-related AHF.

3.1.2 Estimating Traffic Heat Flux

Q_{traffic} is estimated based on a bottom-up approach (Khalifa et al., 2016; Sailor & Lu, 2004) (Equation 4):

$$\begin{aligned} Q_{\text{traffic}} &= \frac{E_{\text{total}}}{A_{\text{improad}}} \\ &= \frac{E_{\text{vehicle}} \cdot N_{\text{lane}} \cdot Flow_{\text{vehicle}}}{Speed_{\text{vehicle}} \cdot Width_{\text{improad}} \cdot 3600}, \end{aligned} \tag{4}$$

where E_{total} is the total traffic heat release rate (W) on the impact area of impervious road A_{improad} (m^2). E_{vehicle} is the heat release rate per vehicle (W), N_{lane} is the number of vehicle lanes, $Flow_{\text{vehicle}}$ is the number of vehicles per hour per lane (vehicles/hour-lane), $Speed_{\text{vehicle}}$ is the vehicle speed (m/s), and $Width_{\text{improad}}$ is the width of impervious road.

N_{lane} is calculated as (Equation 5):

$$N_{\text{lane}} = \begin{cases} 0, & \frac{Width_{\text{improad}}}{Width_{\text{lane}}} < 0.5 \\ 1, & 0.5 \leq \frac{Width_{\text{improad}}}{Width_{\text{lane}}} < 1 \\ \left\lfloor \frac{Width_{\text{improad}}}{Width_{\text{lane}}} \right\rfloor, & \end{cases} \tag{5}$$

where $Width_{\text{lane}}$ is a constant of 3.5 m. The floor function $\lfloor\rfloor$ returns the greatest integer less than or equal to a given number. If the result is an odd number larger than 1, 1 is subtracted to ensure an even number of lanes. As a result, N_{lane} could be 0, 1, 2, 4, and 6 (Figure C1). The remaining width ($Width_{\text{improad}} - Width_{\text{lane}} \cdot N_{\text{lane}}$) is assumed to be allocated to impervious road surface for pedestrians.

$Width_{\text{improad}}$ is calculated as (Equation 6):

$$Width_{\text{improad}} = \left(\frac{H_{\text{roof}}}{HWR}\right) \cdot (1 - F_{\text{perroad}}), \tag{6}$$

where H_{roof} is the roof height, HWR is the canyon height-to-width ratio, and F_{perroad} is the fraction of pervious road. H_{roof}, HWR, and F_{perroad} come from CESM's default land surface datasets (`https://svn-ccsm-inputdata.cgd.ucar.edu/trunk/inputdata/lnd/clm2/`). Although N_{lane} and $Width_{\text{lane}}$ could potentially be derived from real-world road network datasets such as OpenStreetMap (Haklay & Weber, 2008), we choose to use the CLMU's default morphological parameters to maintain consistency with CESM's urban representation. This approach allows us to link traffic heat flux estimates directly with the urban land surface characteristics represented in CESM, rather than relying on potentially inconsistent or regionally variable external datasets.

Except for these two morphological parameters (i.e., N_{lane}, $Width_{\text{improad}}$), the rest of the parameters (i.e., E_{vehicle}, $Flow_{\text{vehicle}}$, $Speed_{\text{vehicle}}$) are time-varying. Specifically, E_{vehicle} is determined by the mix of vehicle types, including ICEVs using gasoline, diesel, HEVs, and EVs. The proportion of each vehicle type is shaped by technological advancements and policy regulations, and varies widely by region over time. For example, gasoline vehicles dominate in the U.S., diesel vehicles have historically been more common in Europe, and new energy cars are rapidly gaining popularity in China (International Energy Agency (IEA), 2024). Accordingly, grouping fuels into gasoline and diesel captures major global preferences, while accounting for HEVs and EVs reflects their growing market shares. These variations highlight the importance of not relying on a single vehicle type assumption in GCMs/ESMs, as doing so would overlook critical regional differences in energy use and emissions. Accordingly, E_{vehicle} is weighted by the vehicle fractions (Equation 7):

$$E_{\text{vehicle}}(y) = \frac{\sum p_v(y) \cdot E_v \cdot R_{\text{v}}}{\sum p_v(y)}, \tag{7}$$

where $p_v(y)$ indicates the fraction of a certain vehicle type v in a certain year y, E_v indexes the total energy generation rate of a certain vehicle type v, R_{v} is the energy waste ratio, and $\sum p_v(y) = 1$.

Vehicle energy profiles vary by vehicle types (Table 2). For ICEVs, energy generation is calculated as the product of the heat of fuel combustion (λ_{fuel}) and the fuel mass rate (m_{fuel}) in the engine ($E_v = \lambda_{\text{fuel}} \cdot m_{\text{fuel}}$) (Prusa et al., 2002). We assumed E_v for gasoline and diesel vehicles as 45 mJ/kg $\cdot$ 0.6 g/s = 27 kW, and 42.5 mJ/kg $\cdot$ 0.7 g/s = 29.75 kW, respectively. The net heat of gasoline combustion of 45 mJ/kg is derived from Sailor and Lu (2004), slightly lower than Smith et al. (2009)'s assumption of 45.85 mJ/kg. The 42.5 mJ/kg is derived from Lee et al. (2017), also lower than Smith et al. (2009)'s assumption of 46 mJ/kg. The E_v of EV at a vehicle speed range from 20 to 40 km/h is assumed at 5.6 kW (Ivanchev et al., 2020). This value is close to Y. Xie et al. (2020)'s estimation of energy consumption of 14.53 kWh/100 km at 25°C. HEV is assumed to be 40% of gasoline and 60% of electricity, leading to the E_v of 14.16 kW. We set R_{v} for gasoline and diesel as 0.7 and 0.65, respectively, as direct thermal loss accounted for more than 0.77 in a driving scenario of urban light snow (Prusa et al., 2002). According to Ivanchev et al. (2020), EV is six times more efficient than ICEVs, we set R_{v} as 0.12 for EV, closer to Ayartürk et al. (2016)'s estimation of up to 0.15. Compared to conventional ICEVs, the energy consumption of EVs is temperature-dependent (Skuza & Jurecki, 2022). We applied a time-varying temperature scaler SFT(t) to adjust EV's heat release to the air (Donkers et al., 2020; Y. Xie et al., 2020) (Equation 8):

$$\text{SFT}(t) = \begin{cases} 1.0 + 0.0165 \cdot (20 - T(t)), & 0 < T(t) < 20 \\ 1.33, & -10 < T(t) \leq 0 \\ 1.4, & -20 < T(t) \leq -10 \\ 1.58, & T(t) \leq -20 \end{cases} \tag{8}$$

where t index model time, $T(t)$ is the atmospheric temperature (°C) at certain time of t.

Table 2. Vehicle Energy Profiles.

Vehicle type	Energy generation rate (E_v, unit: kW)	Energy waste ratio (R_{v}, unitless)	Vehicle heat release ($E_v \cdot R_{\text{v}}$, unit: kW)
Gasoline	27	0.7	18.9
Diesel	29.75	0.65	19.34
Hybrid electric	14.16	0.37	5.24
Electric	5.6	0.12	0.67·SFT

[1] Final electric vehicle heat release is weighted by the temperature scaler (SFT) (Equation 8).

[2] We acknowledge that the estimation of E_v is based on the fuel economy of an average fleet. Actual energy consumption varies by vehicle type, powertrain characteristics, and operational conditions such as speed. Similarly, R_{v} of ICEVs may be lower in the future due to the improvements in fuel economy, potentially narrowing the difference between ICEVs and EVs.

[2] Users may customize the values of $E_v \cdot R_{\text{v}}$ based on specific vehicle fleet compositions or future technology scenarios to better suit their applications.

$Speed_{\text{vehicle}}$ is influenced by secondary weather impacts such as precipitation and snow. Rain and snow reduce road friction, leading to lower speeds due to cautious driving (Billot et al., 2009; Jägerbrand & Sjöbergh, 2016; Padget et al., 2001). Rakha et al.

(2012) found that rain precipitation of 3 mm/h (∼0.00083 mm/s) and 15 mm/h reduced light-duty vehicle speed by 5% and 8%, respectively. C. Liu et al. (2017) found the average vehicle speed reduction of 6% when rain intensity was over 6.35 mm/h. That is, $Speed_{\text{vehicle}}$ is calculated as (Equation 9):

$$Speed_{\text{vehicle}}(t) = Speed \cdot \text{SFRain}(t) \cdot \text{SFSnow}(t), \tag{9}$$

where $Speed$ is a constant of 11.1 m/s (∼40 km/h), as suggested by the World Health Organization World Health Organization (2018) and Pigeon et al. (2008), SFRain_t is the scale factor of adjusting the $Speed$ based on atmospheric rain, and SFSnow_t is the scale factor based on atmospheric snow. The SFRain_t from Rakha et al. (2012)'s empirical experiments is (Equation 10):

$$\text{SFRain}(t) = \begin{cases} 1.0 - 60 \cdot Rain(t), & 0 < Rain(t) \leq 0.00083 \\ 1.0 - (90 \cdot Rain(t) + 0.0425), & Rain(t) > 0.00083 \\ 1.0, & Rain(t) = 0 \end{cases} \tag{10}$$

where $Rain(t)$ is the atmospheric rain (mm/s) at certain time of t. Based on C. Liu et al. (2017), SFSnow(t) is (Equation 11):

$$\text{SFSnow}(t) = \begin{cases} 0.96, & 0 < Snow(t) \leq 0.000353 \\ 0.92, & 0.000353 < Snow(t) \leq 0.000706 \\ 0.91, & 0.000706 < Snow(t) \leq 0.00353 \\ 0.87, & Snow(t) > 0.00353 \\ 1.0, & Snow(t) = 0 \end{cases} \tag{11}$$

where $Snow$(t) is the atmospheric rain (mm/s) at certain time of t.

$Flow_{\text{vehicle}}$ represents vehicle flow as a parameter varying with model time t and urban landunit class l. In CTSM, urban landunits are classified as tall building districts (TBD), high-density (HD), and medium-density (MD) urban areas. Traffic volumes are typically higher in tall building districts compared to high-density and medium-density urban areas. Moreover, traffic tends to peak during the morning and late afternoon hours. To capture these temporal and spatial differences, we introduced a scale factor SF(h) to represent diurnal variations of traffic flow (Equation 12):

$$Flow_{\text{vehicle}}(l, t) = \text{AADT}(l, y) \cdot \text{SF}(h), \tag{12}$$

where AADT(l, y) (unit: vehicles/day-lane) denotes the annual average daily traffic volume per lane in a certain urban landunit class l for a certain year of y. SF(h) is the scale factor at hour h of the day. We have not considered the snowfall impact on vehicle flow yet, given the complex urban operations such as snow removal (Tanimura et al., 2015). Seasonal variations in travel activity are also not incorporated, due to the diversity of climate zones represented globally. Additionally, users should be aware of road capacity when customizing traffic inputs. For example, a sub-region of downtown San Francisco observed the road network capacity of $Flow_{\text{vehicle}}$ at 750 vehicles/hour-lane (L. Jin et al., 2024).

3.2 Model Modification

We adopted the existing namelist option "urban_traffic" to allow users to enable the traffic module "UrbanVehicleType" in CESM's land component, the Community Terrestrial Systems Model (CTSM) (Oleson & Feddema, 2020). The "urban_traffic" has been set to ".false." in all previous versions of CTSM, excluding traffic heat from calculating urban surface energy balance.

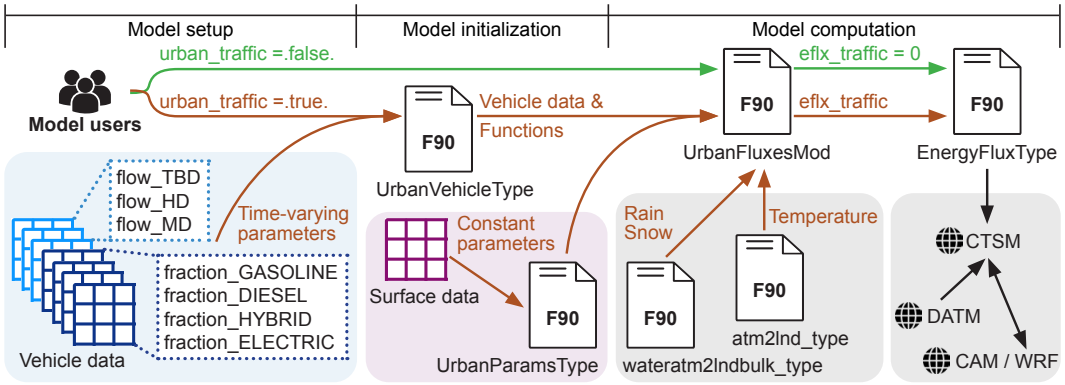

Figure 2. Workflow of incorporating urban traffic modeling in the Community Terrestrial Systems Model (CTSM). CTSM is the land component of the Community Earth System Model (CESM). In the land-only model, CTSM is driven by atmosphere forcing data (DATM), whereas in the coupling mode, CTSM has been coupled to the Community Atmosphere Model (CAM) or Weather Research and Forecasting (WRF).

When users set "urban_traffic" as ".true.", the new module performs two key functions: reading time-varying traffic inputs and providing relevant computational routines (Figure 2). Specifically, a separate input stream data file provides seven parameters, where "flow_*" denotes AADT for three urban landunits (i.e., TBD, HD, and MD) and "fraction_*" denotes p_v for four vehicle types (i.e., gasoline, diesel, hybrid electric, electric). At the model initialization stage, the "UrbanVehicleType" module initializes time-varying AADT and vehicle fraction. Meanwhile, the "UrbanParamsType" module initializes urban constant parameters from surface data. In the "UrbanParamsType" module, we incorporated new code to quantify N_{lane} and $Width_{\text{improad}}$ based on Equation 5 and 6, respectively. Using the vehicle time-varying input data and supporting functions from "UrbanVehicleType", the "UrbanFluxesMod" module calculates the "eflx_traffic", where we designed traffic to enter the canyon floor, thereby first influencing the ground (soil) temperature. This approach differs from models where anthropogenic heat is directly added to the canyon air to affect air temperature directly, such as in the Common Land Model-Urban (CoLM-U) (`https://github.com/yuanhuas/CoLM-U/blob/master/main/UrbanFlux.F90`) or added to the sensible heat flux, such as in WRF-NOAH-SLUCM (`https://github.com/wrf-model/WRF/blob/master/phys/module_sf_urban.F`). The "eflx_traffic" is subsequently passed to "EnergyFluxType" for integration into the land energy budget computations within CTSM.

As a land surface model, CTSM can operate in a land-only configuration driven by the data atmosphere model (DATM), or coupled with CAM, enabling two-way land-atmosphere interactions. Additionally, the WRF-CTSM coupling technique presents potential for applying the new traffic heat module in regional climate simulations with an interactive atmosphere model (CTSM Development Team, 2024a; Mužić et al., 2025).

3.3 Model Validation

We ran single-point simulations in CTSM with the version tag "ctsm5.3.024" for model validation at two sites. Sites were selected based on the availability of historical observations for both environmental variables and traffic conditions (Table 3). The first site, FR-Capitole (Section 3.3.1), was chosen from the Urban-PLUMBER model evaluation project, which provides flux tower data across 21 urban sites (M. J. Lipson et al., 2023). We matched this flux tower location with the nearest traffic detectors from the

UTD19 dataset (Loder et al., 2019). Since Urban-PLUMBER observations lack temperature and humidity data, we selected UK-Manchester (Section 3.3.2) as a second validation site to evaluate the model's performance in simulating air temperature and relative humidity using available sensor data.

Table 3. Experiment Design.

Feature		Case study 1		Case study 2	
Site name		FR-Capitole (43.6035°N, 1.4454°E)		UK-Manchester (53.4808°N, 2.2328°W)	
City		Toulouse, France		Manchester, UK	
Köppen-Geiger climate zone (1991–2020) (M. J. Lipson et al., 2023)		Cfa (Temperate, no dry season, hot summer)		Cfb (Temperate, no dry season, warm summer)	
Observation	Environmental measurement	Flux tower from the Urban-PLUMBER (M. J. Lipson et al., 2023)		Low-cost sensor (Y. Sun, Bannan, et al., 2025)	
	Variables for model validation	Radiation and turbulent fluxes (i.e., SW_{up}, LW_{up}, Q_{h}, Q_{le}, Q_{tau})		Near-surface air temperature (T_{air}) and relative humidity (RH)	
	Traffic monitor	A detector on the road from a global urban traffic dataset, UTD19 (Loder et al., 2019)		A VivaCity camera from Transport for Greater Manchester (TfGM)	
Simulation	Period for model spin-up	1 January 1994 to 20 February 2004		1 January 2012 to 31 December 2021	
	Period for data analysis	20 February 2004 to 28 February 2005		1 January 2022 to 31 December 2022	
	T_BUILDING_MIN	11.95°C		16.95°C	
	T_BUILDING_MAX	26.85°C		26.85°C	
	p_ac	0.047		0.018	
	Simulation name	CNTL	TRAF	CNTL	TRAF
	Traffic configuration	urban_traffic = .false.	urban_traffic = .true.	urban_traffic = .false.	urban_traffic = .true.

[1] T_BUILDING_MIN is the minimum interior building temperature, acting as a CLMU's building space heating threshold to simulate Q_{heat}.

[2] T_BUILDING_MAX is the maximum interior building temperature, acting as a baseline threshold of air conditioning.

[3] p_ac is the air-conditioning penetration rate. The simulated Q_{ac} is determined by both T_BUILDING_MAX and p_ac (Li, Zhao, Oleson, et al., 2024).

[4] T_BUILDING_MIN, T_BUILDING_MAX and p_ac come from CTSM's default input dataset.

[5] CNTL refers to the control simulation using the default model source code. TRAF uses the same configuration as CNTL, except with the traffic heat module enabled.

3.3.1 Case Study 1: Capitole of Toulouse, France

A flux tower site of Capitole, France (43.6035°N, 1.4454°E) participated in the Urban-PLUMBER project, hereinafter referred to as FR-Capitole (M. J. Lipson et al., 2023). FR-Capitole is located in the center of Toulouse with a 500 m observational footprint. Its background climate is classified as temperate, with no dry seasons, and a hot summer (Beck et al., 2023).

Single-point simulations at the FR-Capitole site started from 1 January 1994 to 1 March 2005, where data for analysis began from 20 February 2004 (Goret et al., 2019; Masson et al., 2008). Model configuration and urban parameter input in the CNTL simulation were kept consistent with Urban-PLUMBER, where CTSM was forced by atmosphere data with a 30-minute interval. Urban-PLUMBER provided urban morphological and albedo parameters. The rest parameters were from CTSM5.3's default land surface data (Table D1). As its local building height averaged around 15 m (Goret et al., 2019), we set the PCT_URBAN as 100% for the medium-density urban class. CLMU's building energy model quantified Q_{ac} whenever indoor air temperature exceeds 26.85°C and Q_{heat} whenever the indoor temperature drops below 11.95°C.

We ran a TRAF simulation with only the difference of enabling our newly developed module. Traffic data at this site came from a global traffic dataset, UTD19 (Loder et al., 2019), from which a traffic detector (43.604907°N, 1.445499°E) was close to the FR-Capitole site (Figure 3(a)). The sensor detected traffic flow every Friday since 16 May 2008, for seven weeks at a 3-minute interval, providing vehicle flow per hour per lane. Daily traffic volume for these seven Fridays was 4939, 4475, 3853, 4405, 4664, 5059, and 3434 vehicles/day-lane, respectively. We calculated the AADT as 4404 vehicles/day-lane, and extracted the diurnal profile averaged from UTD19 data, where the percentage of AADT peaked at 7.8% at 8:00 and dropped to the bottom at 0.6% at 4:00 (Figure 3(b)). This diurnal cycle was similar to Pigeon et al. (2007)'s, which ranged from a minimum of 0.4% at 03:00 to a maximum of 7.3% at 08:00 during weekdays based on 21 observation sites in Toulouse. Due to a lack of real-time traffic data, we assumed the vehicle fleet composition in 2004 to consist of 40.6% gasoline, 59.4% diesel, 0% hybrid electric, and 0% electric vehicles. For comparison, the average passenger cars in use in France in 2019 were composed of 40.2% gasoline, 58.5% diesel, 0.7% hybrid electric, and 0.4% electric vehicles (European Automotive Manufacturers Association, 2021). $Width_{\mathrm{improad}}$ was 8.4 m and N_{lane} was 2.

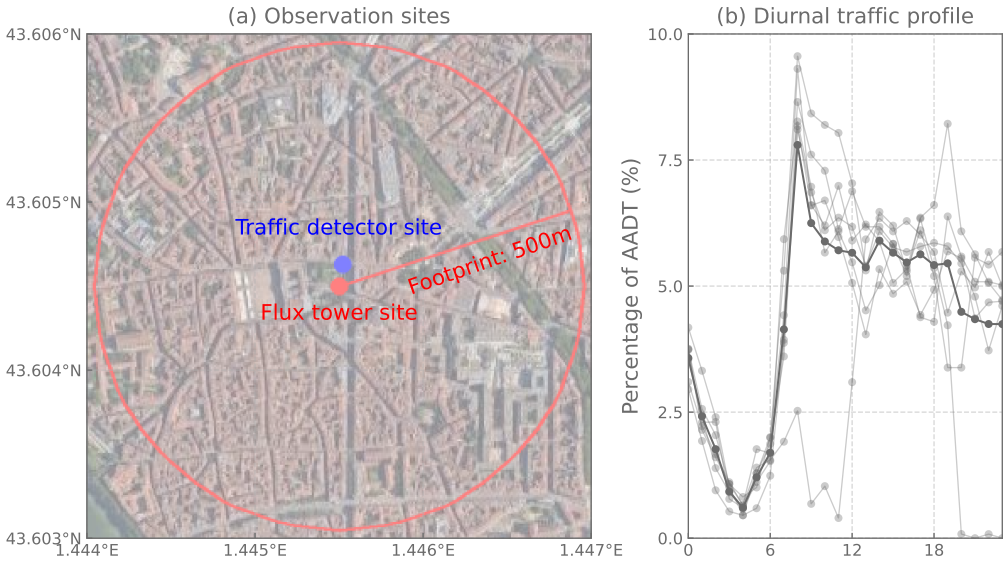

Figure 3. Case study of Capitole of Toulouse, France (FR-Capitole). (a) Observation sites. (b) Diurnal fraction of annual average daily traffic volume (AADT).

3.3.2 Case Study 2: Manchester, UK

Greater Manchester had multiple low-cost sensors monitoring air pollution, which provided near-surface air temperature (T_{air}) and relative humidity (RH) (Y. Sun, Bannan, et al., 2025). We selected one QuantAQ sensor at Dale Street (53.4808°N, 2.2328°W), a commercial space closer to the city center, hereinafter referred to as UK-Manchester (Figure 4(a)). Its background climate is classified as temperate, with no dry season, and a warm summer (Beck et al., 2023).

We spun up the model from 1 January 2012 to 31 December 2021, followed by one year for data analysis. Atmospheric forcings were derived from the ERA5-Land reanalysis data at an hour interval, with bias correction. According to local climate zone classification, the site is built as LCZ 2 of compact mid-rise (Demuzere et al., 2022). Thus,

we set the PCT_URBAN as 100% for the medium-density urban areas. The building height was 26 m, extracted from the Global Human Settlement Layer (GHSL) dataset (Pesaresi & Politis, 2022). Except for building height, the rest of the urban parameters came from the CTSM5.3's default dataset (Table D1). Traffic flow data came from a Transport for Greater Manchester (TfGM) Vivacity camera, which was close to the QuantAQ sensor (Figure 4(b)). The AADT average based on hourly traffic flow data in 2022 was 4697 vehicles/day-lane. As a commercial area, the diurnal cycle of the UK-Manchester site showed a peak hour at 17:00. $Width_{\mathrm{improad}}$ was 10.7 m and N_{lane} was 2. In 2022, the average car composition in the UK was 58.2% gasoline, 34.7% diesel, 4.9% hybrid electric, and 2.1% electric vehicles (European Automotive Manufacturers Association, 2024). However, the EVs share in Manchester remained at just 1% (Manchester city council, 2022). Accordingly, we assumed the vehicle fleet to consist of 59.4% gasoline, 34.7% diesel, 4.9% hybrid electric, and 1.0% electric vehicles at the UK-Manchester site.

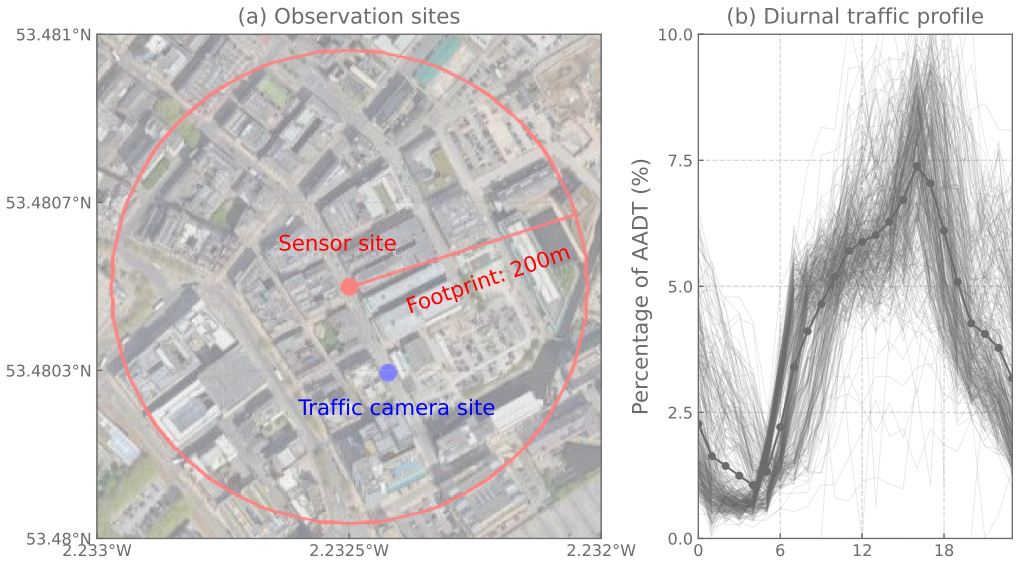

Figure 4. Case study of Dale Street, Manchester, UK (UK-Manchester). (a) Observation sites. (b). Diurnal fraction of annual average daily traffic volume (AADT).

Given that the UK experienced a record-breaking temperature in the 2022 summer, we identified two heatwaves from 17 to 19 July and from 9 to 15 August 2022 at the UK-Manchester site according to the Met Office, a heatwave in Manchester was defined as at least three consecutive days with daily maximum temperatures exceeding 25°C (Met Office, n.d.). To assess the human heat stress amplified by traffic heat during urban heatwaves, we selected three human heat stress indicators, including the 2 m US National Weather Service Heat Index (NWS_HI), quantified by Equation D1, 2 m simplified Wet-Bulb Globe Temperature (sWBGT) quantified by Equation D2 and 2 m Discomfort Index (DI) by Equation D3.

3.4 Model Sensitivity Analysis

To evaluate the model's sensitivity to traffic intensity, we conducted an idealized experiment by applying perturbation factors of ±10%, ±20%, ±40%, and ±80% to AADT. This sensitivity test did not consider roadway capacity constraints and was not intended

to represent realistic traffic flows, but rather to assess how the model responds to changes in traffic volume.

Simulations were performed for two representative weeks, one in summer and one in winter, at each study site. For the FR-Capitole site, simulations were carried out from 27 June to 4 July 2004 (summer) and from 2 January to 9 January 2005 (winter). For the UK-Manchester site, the simulation periods were from 16 July to 23 July 2022 (summer) and from 10 December to 17 December 2022 (winter).

The total of 8 perturbations for 2 periods at 2 sites were compared to observations and summarized in Taylor diagrams (Taylor, 2001). Taylor diagrams display the relationship between these datasets, illustrating the normalized standard deviation σ (Equation D4), correlation coefficient ρ (Equation D5), and centered root-mean square difference E' (Equation D6).

4 Result and Discussion

This section describes the results of model validation and sensitivity analysis. Section 4.1 and Section 4.2 show model validation results at FR-Capitole and UK-Manchester sites, respectively. Section 4.3 compares the different traffic-induced thermal impacts between the two sites. Section 4.4 summarizes variations of urban variables by perturbing traffic flow.

4.1 Traffic-Induced Thermal Effects at FR-Capitole

For simulations at the FR-Capitole site, the incorporation of urban traffic modeling showed great improvement of sensible heat flux (Q_{h}) (Figure 5(a), (b)). An annual mean traffic heat flux (Q_{traffic}) of 22.23 W/m^2 from February 2004 to February 2005 resulted in a 15.78 W/m^2 increase in simulated annual average Q_{h}. As Q_{h} in the CNTL simulation was generally underestimated, adding traffic heat narrowed the underestimation throughout the year and aligned well with the observed Q_{h}, particularly from May to October. This reduced the RMSE of the monthly mean Q_{h} from 29.6 W/m^2 in the CNTL simulation to 17.0 W/m^2 in the TRAF simulation, representing a 43% reduction in error. Latent heat flux (Q_{le}) also showed reduced RMSE, where Q_{le} in the TRAF simulation was higher than in the CNTL simulation by an annual average of 1 W/m^2 (Figure 5(c), (d)). In summer, Q_{le} in the TRAF simulation was lower than in the CNTL simulation, as indicated by negative ΔQ_{le} values. Q_{le} represented the energy used for water evaporation, which was primarily governed by moisture availability. Traffic-induced surface and near-surface warming increased ground temperature (T_{grd}) and near-surface air temperature (T_{air}), reducing relative humidity and surface moisture. This drier environment limited evaporation, thereby decreasing Q_{le}. In contrast, in cooler seasons when T_{grd} was more moderate, evaporation was less moisture-limited, allowing for an increase in Q_{le}, reflected in positive ΔQ_{le}. As the inclusion of traffic heat modeling increased the Q_{h}, the simulated Q_{tau} showed a slight rise (Figure 5(e), (f)). This impact on Q_{tau} remained minor, as Q_{tau} was primarily driven by surface roughness (Y. Sun, Oleson, et al., 2025). In addition, the upward solar radiation (SW_{up}) remained unaffected, as it is determined by the surface albedo (Figure 5(g), (h)).

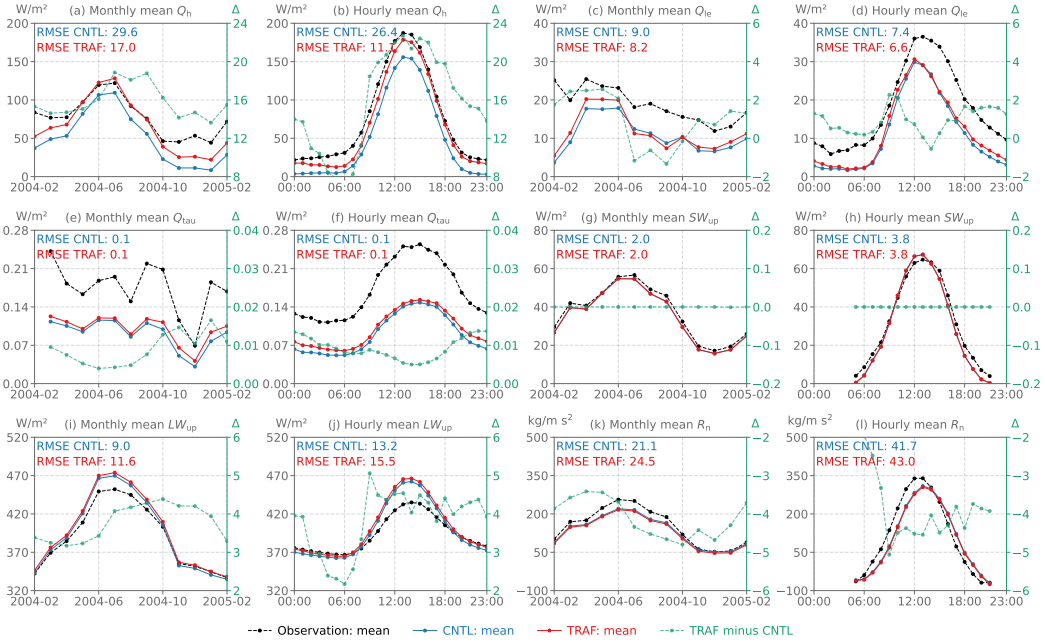

Figure 5. Monthly mean and hourly mean radiative, turbulent, and momentum fluxes at the FR-Capitole site in the CNTL, and TRAF simulations in comparison with observations. (a)–(b) Sensible heat flux (Q_{h}). (c)–(d) Latent heat flux (Q_{le}). (e)–(f) Momentum flux (Q_{tau}). (g)–(h) Upward solar radiation (SW_{up}). (i)–(j) Upward longwave radiation (LW_{up}). (k)–(l) Net radiation on urban surfaces (R_{n}). The root-mean-square error (RMSE) measures the average magnitude of the errors between modeled and observed values. RMSE closer to 0 is better. Some lines representing the CNTL and TRAF simulations overlap in the panels. The left y-axis shows the observed or model variables. The right y-axis shows the difference (Δ) between the TRAF and CNTL simulations.

Despite that adding traffic heat reduced the underestimation of Q_{h} and Q_{le}, the TRAF simulation showed higher longwave radiation flux (LW_{up}) (Figure 5(i), (j)) and lower net radiation flux (R_{n}) (Figure 5(k), (l)), particularly in summer, resulting higher RMSE compared to the CNTL simulation. Given that LW_{up} is determined by surface temperature, the overestimation of LW_{up} suggests that the surface is overheated. This is influenced by both model physics and parameters. Firstly, due to the default setting emissivity of impervious road and pervious road, as 0.97 and 0.99, were rather high than the normal range of 0.9–0.95, LW_{up} was already overestimated in the CNTL simulation. With the added Q_{traffic}, the T_{grd} further increased, leading to higher LW_{up}. Using high-resolution urban parameters dataset such as U-Surf (Cheng et al., 2025) helps refine these estimates. Secondly, the underestimated Q_{le} was constrained by the simplified parameterization scheme for urban pervious surfaces, which omitted the transpiration effects of urban vegetation. Weak urban vegetation effect is likely to increase heat storage and warm the ground. This limitation has been acknowledged by previous studies (e.g. Y. Sun, Oleson, et al., 2025). Finally, Q_{traffic}, combined with building space heating flux (Q_{heat}), and waste heat flux (Q_{w}), was assumed to go into the urban canyon floor, warming the road surface before transferring the heat into the urban canopy air.

Adding Q_{traffic} showed notable increases in the simulated AHF, where the annual average AHF in the TRAF simulation was 27.91 W/m^2 and the maximum reached 85.53 W/m^2 on 28 January 2005 (Figure 6(a), (b)). Q_{traffic} of 22.23 W/m^2 contributed 80.2% of AHF (Figure 6(c), (d)). Comparatively, in the CNTL simulation, the annual average

AHF during 2004–2005 was 6.45 W/m^2, which only came from CLMU's building energy model. In the building sector, AHF mainly appeared in winter due to building space heating, where the daily mean building space heating flux (Q_{heat}) reached a maximum of 39.8 W/m^2 (Figure 6(g), (h)). Air conditioning heat flux was minimal and occurred primarily in the afternoon and at night, when the urban surface had absorbed heat during the day and indoor environments required cooling (Figure 6(f)). The traffic warming effect also influenced building energy consumption. In summer, more air-conditioning and ventilation were required, where monthly mean Q_{ac} increased by up to 0.06 W/m^2 (Figure 6(e)) and Q_{v} by 0.15 W/m^2 (Figure 6(i)). In winter, less building space heating was required to maintain the indoor temperature above the model's critical threshold of indoor minimum temperature, where the monthly mean Q_{heat} was reduced by up to 2 W/m^2. The elevated canopy air temperature, combined with stable indoor temperature, narrowed the outdoor-indoor temperature gradient. This weakened the ventilation intensity, leading to a reduction in monthly mean Q_{v} by 0.3 W/m^2 in January 2005. Located in a temperate climate zone, FR-Capitole experienced a greater decrease in building space heating demand than an increase in air conditioning use in response to traffic-induced warming.

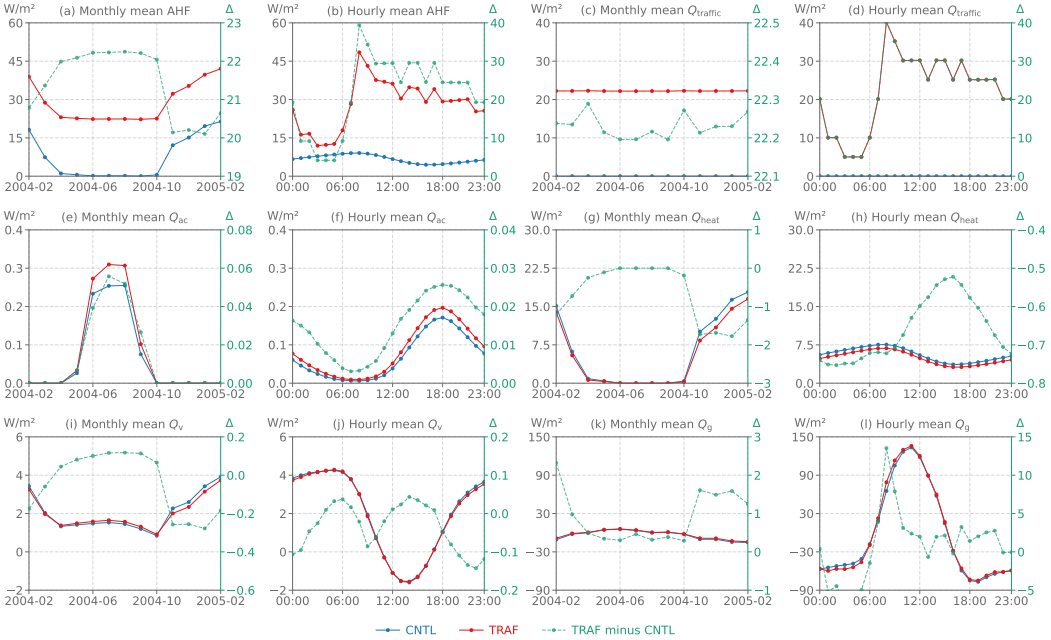

Figure 6. Monthly mean and hourly mean anthropogenic-related fluxes at the FR-Capitole site in the CNTL, and TRAF simulations. (a)–(b) Anthropogenic heat flux (AHF). (c)–(d) Traffic heat flux (Q_{traffic}). (e)–(f) Air conditioning heat flux (Q_{ac}). (g)–(h) Building space heating flux (Q_{heat}). (i)–(j) Building ventilation flux (Q_{v}). (k)–(l) Ground flux (Q_{g}). Some lines representing the CNTL and TRAF simulations overlap in the panels. The left y-axis shows the observed or model variables. The right y-axis shows the difference (Δ) between the TRAF and CNTL simulations.

Online AHF computation using CTSM with the new traffic module show comparability with established AHF dataset. For example, enabling traffic heat modeling computed a maximum monthly mean AHF of 41.23 W/m^2 in February of 2004–2005, closer to 48.22 W/m^2 from A. C. Varquez et al. (2020)'s global 1 km anthropogenic heat gridded dataset (AH4GUC) for the 2010s in a top-down approach (Figure 7(a)). Q_{traffic} con-

tributed to 54.28% of AHF in February whereas more than 90% from April to October. However, Pigeon et al. (2007) found that AHF in the densest urban areas reached 100 W/m^2 in winter during 2004–2005. Such a high AHF has not been detected by the model at the FR-Capitole site yet. Given different approaches to estimate AHF, both simulations had lower monthly mean AHF than the AH4GUC dataset but were higher than Yang et al. (2017)'s 1 km AHF estimation of 0.1 W/m^2 based on nighttime light data in 2010.

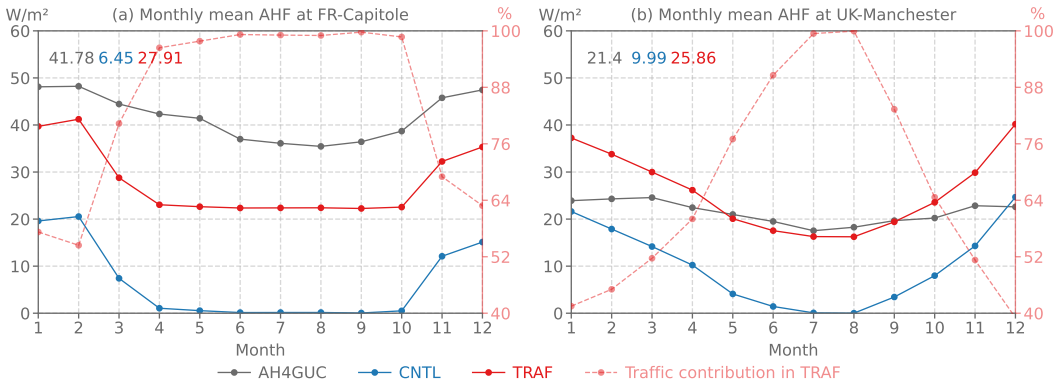

Figure 7. Monthly mean anthropogenic heat flux (AHF) at (a) FR-Capitole during 2004–2005 and (b) UK-Manchester sites in 2022. AH4GUC denotes values from the 1 km dataset for the 2010s (A. C. G. Varquez et al., 2021). Texts on the top are the annual mean AHF from the AH4GUC product, CNTL simulation, and TRAF simulation, respectively. In the TRAF simulation, traffic contribution to AHF is calculated as $100\% \cdot \frac{Q_{\text{traffic}}}{Q_{\text{heat}}+Q_{\text{w}}+Q_{\text{traffic}}}$.

Additionally, Q_{traffic} varied in response to weather conditions, enabling more accurate, event-driven AHF estimates. For instance, on 9 October 2004, heavy rainfall occurred at 17:00, with an intensity of 0.018 mm/s. According to Equation 9, this triggered the model to set the vehicle speed to zero. With no traffic activity, Q_{traffic} dropped to zero. Consequently, that day recorded the lowest daily mean Q_{traffic} value of 21.57 W/m^2. In contrast, the highest daily mean Q_{traffic} of 23.04 W/m^2 occurred on 25 October 2004, during which rainfall persisted from 10:30 into the night. Although vehicle speed was reduced under wet conditions, Q_{traffic} increased due to the continued traffic flow.

4.2 Traffic Impacts on Human Heat Stress during Heatwaves at UK-Manchester

Similarly, the TRAF simulation demonstrates improved performance at the UK-Manchester site, as indicated by lower RMSEs of T_{air} and RH against observations compared to the CNTL simulation. Adding Q_{traffic} increased monthly mean T_{air} by 0.1–0.5°C (Figure 8(a)) and deceased RH by 1–3% (Figure 8(c)). Consequently, the TRAF simulation reproduced a warmer and drier urban environment. The difference in T_{air} between TRAF and CNTL simulation (ΔT_{air}) was higher at night than during the daytime (Figure 8(b)), suggesting peak traffic in the evening was likely to contribute to nocturnal warming. Similar to the FR-Capitole site, Q_{traffic} added to the canyon floor influenced not only temperature but also moisture conditions. Notably, magnitudes of ΔT_{air} were larger in winter than in summer, indicating a stronger seasonal sensitivity to traffic-induced warming under cooler background climate conditions.

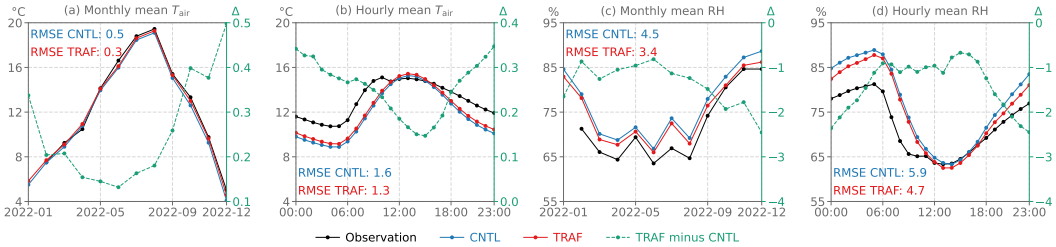

Figure 8. Monthly mean and hourly mean temperature and relative humidity at the UK-Manchester site in the CNTL, and TRAF simulations in comparison with observations. (a)–(b) 2 m air temperature (T_{air}). (c)–(d) 2 m relative humidity (RH). Two shading of heatwaves were from 17 to 19 July and 9 to 14 August 2022, respectively. The root-mean-square error (RMSE) measures the average magnitude of the errors between modeled and observed values. RMSE closer to 0 is better. The left y-axis shows the observed or model variables. The right y-axis shows the difference (Δ) between the TRAF and CNTL simulations.

Anthropogenic-related variables at the UK-Manchester site showed temporal variation patterns similar to those at FR-Capitole. TRAF simulations output an annual mean AHF to 25.86 W/m^2 (Figure 9(a), (b)), consisting of an annual mean Q_{traffic} of 16.27 W/m^2 (Figure 9(c), (d)). This was higher than the annual mean AHF from building energy consumption at 9.99 W/m^2 in 2022 in the CNTL simulation. For reference, A. C. Varquez et al. (2020) estimated an annual mean AHF of 21.4 W/m^2 for the 2010s and K. Jin et al. (2019) of 29.9 W/m^2 for 2015 (Table D2). However, both simulated AHFs were lower than Smith et al. (2009)'s estimation of 50–75 W/m^2 with an additional 8% from metabolism. Due to its colder background climate, the model simulated little air conditioning use in summer, even during the 16–19 July heatwave (Figure 9(e), (f)). In the model, the building space heating operated to maintain the indoor temperature above 16.95°C, which might be a relatively high threshold. Given the sparsely built-up area at the UK-Manchester site, the modeled indoor temperature might be lower due to greater heat loss, causing space heating to remain active longer than expected (Figure 9(g), (h)). As a result, uncertainties in modeling building space heating flux resulted in overestimated AHF in cold months. In December 2022, the monthly mean AHF was 41.1 W/m^2 in the TRAF simulation, higher than AH4GUC's monthly value of 22.6 W/m^2 in December (Figure 7(b)).

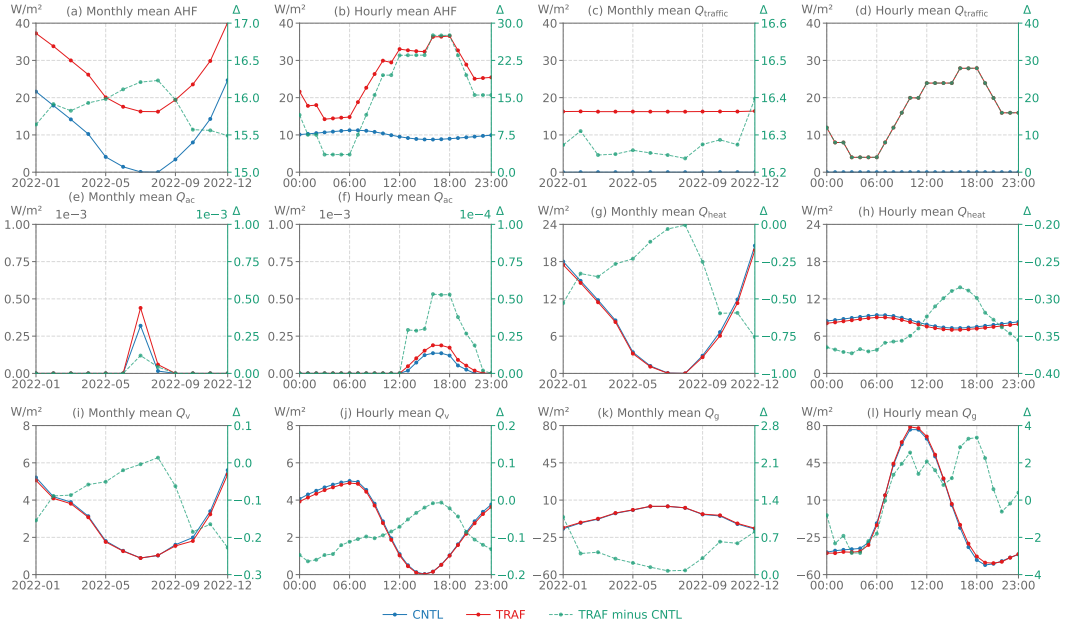

Figure 9. Monthly mean and hourly mean anthropogenic-related fluxes at the UK-Manchester site in the CNTL, and TRAF simulations. (a)–(b) Anthropogenic heat flux (AHF). (c)–(d) Traffic heat flux (Q_{traffic}). (e)–(f) Air conditioning heat flux (Q_{ac}). (g)–(h) Building space heating flux (Q_{heat}). (i)–(j) Building ventilation flux (Q_{v}). (k)–(l) Ground flux (Q_{g}). Some lines representing the CNTL and TRAF simulations overlap in the panels. The left y-axis shows the observed or model variables. The right y-axis shows the difference (Δ) between TRAF and CNTL simulations.

Traffic heat did not noticeably affect the heatwave duration but it did intensify human heat stress during heatwave events. In the TRAF simulation, 2 m US National Weather Service Heat Index (NWS_HI) consistently exceeded that of the CNTL simulation, with ΔNWS_HI reached a maximum of 4.9°C at 23:00 on 17 July (Figure 10(a)) and 5.3°C at 23:00 on 12 August 2022 (Figure 10(b)). This lag between traffic peak and ΔNWS_HI peak stemmed from the natural properties of the urban surface, which absorbed heat during the day and released heat to the canopy air at night. Husni et al. (2022) also noted a temporal delay between traffic flow and its thermal impact on air temperature. Consequently, Q_{traffic} primarily added heat during the late afternoon, keeping canopy air warmer into the night. This reduced the day-night air temperature gradient, therefore elevating nighttime human heat stress during heatwaves. Comparisons between TRAF and CNTL simulations showed that, during the July heatwave, the aggregated NWS_HI hours exceeding the critical "danger" threshold of 40°C increased by 1.9°C·hours. Interestingly, 2 m simplified Wet-Bulb Globe Temperature (sWBGT) and 2 m Discomfort Index (DI) in the TRAF simulation were occasionally lower than in CNTL during the late night and early morning (Figure 10(d), (f)). These reductions were likely due to decreased air moisture in the TRAF simulation, which had a stronger effect on these metrics than temperature during these times. Therefore, although traffic heat increased urban temperature, it did not always result in proportionally higher human heat stress, depending on the metric used and the timing of thermal effects.

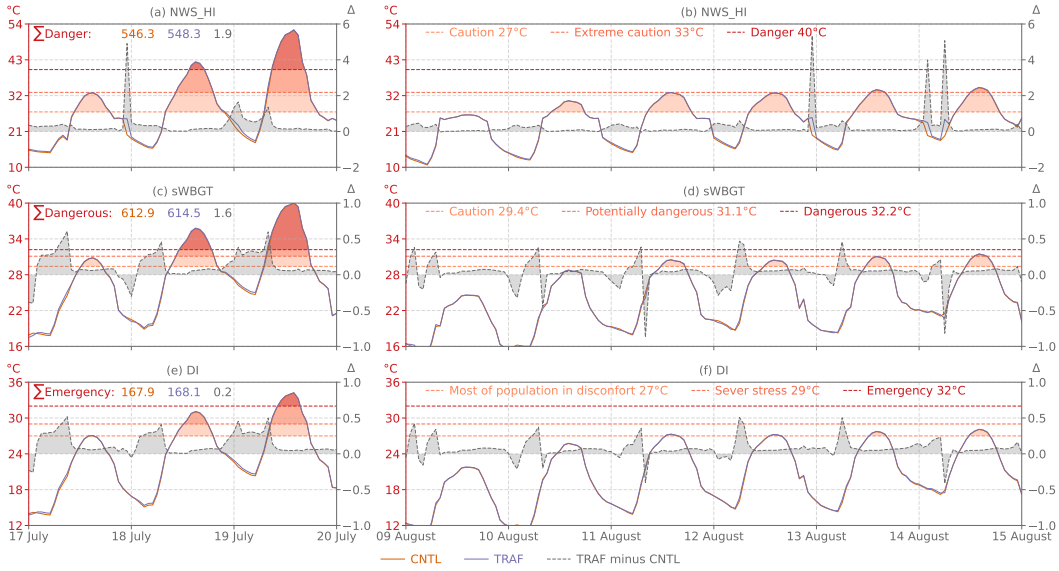

Figure 10. Heat stress variations during two heatwave periods at the UK-Manchester site for the CNTL and TRAF simulations. (a), (b) 2 m US National Weather Service Heat Index (NWS_HI). (c), (d) 2 m simplified Wet-Bulb Globe Temperature (sWBGT). (e), (f) 2 m Discomfort Index (DI). The left y-axis denotes the index values. The right y-axis denotes the differences between the TRAF and CNTL simulations. The text $\sum$ (unit: °C·hours) denotes the cumulative human heat stress burden, calculated as the product of each index and the number of hours exceeding its highest critical threshold.

4.3 Differences in Traffic Heat Impacts between FR-Capitole and UK-Manchester

Both FR-Capitole and UK-Manchester showed traffic-induced urban warming with similar mechanisms but different temporal variations and magnitudes. Q_{traffic} added to the canyon floor first increases T_{grd} of impervious road and pervious road. This rise in T_{grd} enhances LW_{up} and reduces R_{n} under land-only mode (Figure 11). The elevated T_{grd} subsequently warms the canopy air. When the canopy air is warmer than the atmosphere, the increased T_{grd} enhances the temperature gradient between the canopy and the overlaying atmosphere, leading to an increase in Q_{h}. In contrast, during cold seasons in high-latitude regions, when the canopy air is colder than the atmosphere, Q_{h} becomes negative, and its absolute value decreases. Higher T_{air} also affects the indoor thermal environment by raising the T_{grd} of other surfaces (i.e., roof, sunlit wall, shade wall), and then T_{b}. In summer, the earlier exceedance of the indoor maximum temperature triggers the activation of Q_{ac} in CLMU's building energy model, increasing indoor cooling demands. In winter, the rise in T_{b} reduces the deviation from the setting of indoor minimum temperature, leading to lower space heating energy use. We acknowledge that this is an idealized scheme, unlike real-world conditions where traffic heat instantaneously influences road surface temperature through friction, radiation, and convection, and influences wall temperature through convection and radiation (Neog et al., 2021).

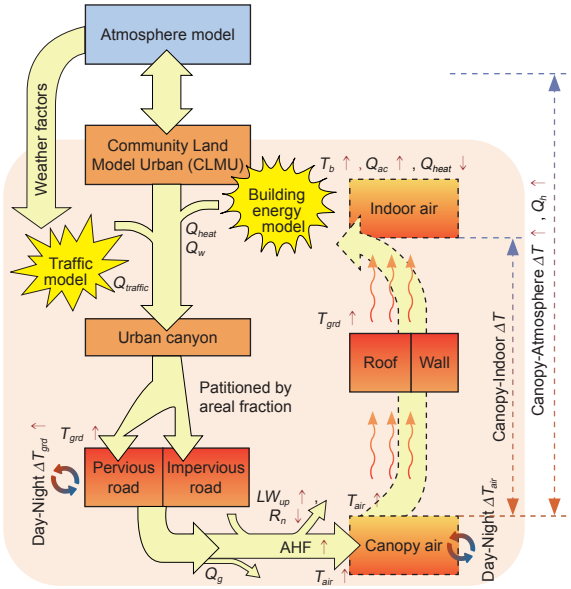

Figure 11. Biogeophysical mechanism of traffic-induced thermal effects based on model assumptions.

Despite similar annual average daily traffic volumes—4404 and 4697 vehicles/day-lanes—at the FR-Capitole and UK-Manchester sites, respectively, their annual average Q_{traffic} differed at 22.23 and 16.27 W/m^2 due to differences in vehicle types (Table 4). Variations in urban surface properties, background climate, and traffic diurnal cycle could further contribute to the distinct temperature responses from the urban ground, canopy air, and indoor air between the two cities.

Table 4. Traffic-Induced Daily Mean Temperature Differences between TRAF and CNTL Simulations.

Site name	FR-Capitole			UK-Manchester		
Year of simulation	2004			2022		
Traffic volume (unit: vehicles/day-lane)	4404			4697		
Metrics of simulation ouputs	ANN mean	JJA mean	DJF mean	ANN mean	JJA mean	DJF mean
Vehicle speed ($Speed_{\text{vehicle}}$, unit: m/s)	11.08	11.09	11.08	11.06	11.08	11.03
Traffic heat flux (Q_{traffic}, unit: W/m^2)	22.23	22.2	22.24	16.27	16.24	16.33
Traffic-induced ground temperature changes (ΔT_{grd}, unit: °C)	0.64	0.58	0.69	0.38	0.29	0.46
Traffic-induced 2 m canopy air temperature changes (ΔT_{air}, unit: °C)	0.4	0.3	0.5	0.25	0.16	0.35
Traffic-induced indoor air temperature changes (ΔT_{b}, unit: °C)	0.27	0.42	0.0	0.05	0.14	0.0

[1] ANN, JJA, and DJF denotes annual, June-July-August, and December-January-February, respectively.

[2] Δ denote TRAF minus CNTL.

Densely built-up areas were more likely to experience greater traffic-induced temperature increases compared to sparsely built-up areas under similar traffic volumes. Dur-

ing summer, FR-Capitole experienced a mean increase of 0.3°C in T_{air} and 0.42°C in T_b comparing TRAF to CNTL simulations (Figure 12(a)), whereas UK-Manchester saw similar increases of 0.16°C in T_{air} and 0.14°C in T_b due to traffic heat, respectively (Figure 12(c)). From the view of urban morphology, FR-Capitole featured a denser urban representation, characterized by a canyon height-to-width ratio (CANYON_HWR) of 1.32, a high fraction of roof (WTLUNIT_ROOF) of 0.62, and a small pervious road fraction (WTROAD_PERV) of 0.26 (Table D1). These morphological parameters depicted a narrow canyon, dense buildings, and limited pervious roads, promoting greater heat retention within both the canyon and indoor spaces. Consequently, indoor temperatures rose more than outdoor ones, by 0.4–0.45°C (Figure 12(a)). In contrast, the magnitude of temperature increases due to traffic at UK-Manchester was lower (Figure 12(c)). It was characterized by a wider canyon (CANYON_HWR = 0.75), lower building density (WTLUNIT_ROOF = 0.35), and more pervious road (WTROAD_PERV = 0.69), which allowed heat to escape more easily.

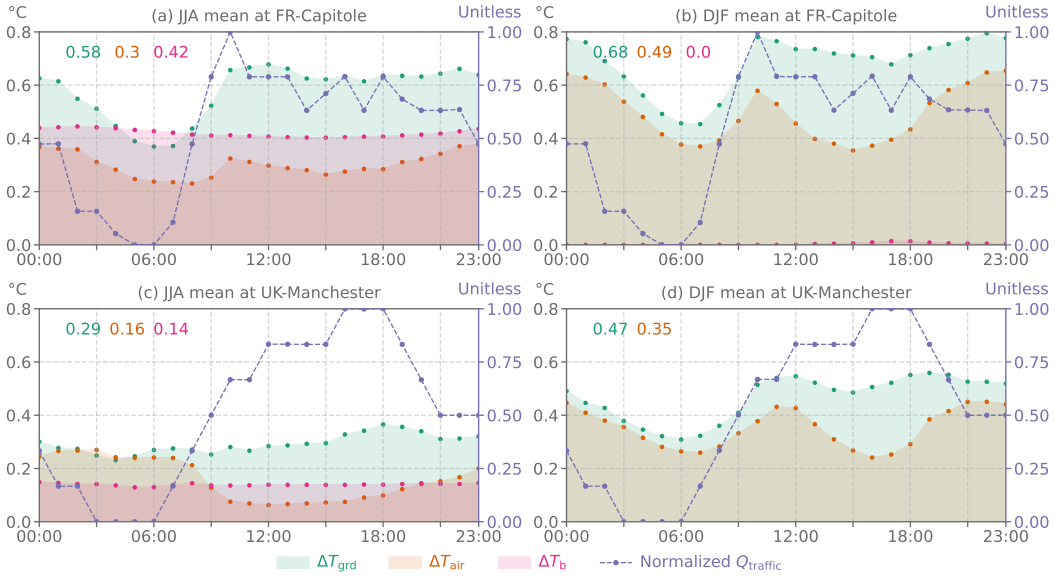

Figure 12. Diurnal variations (local time) of the differences in ground temperature (ΔT_{grd}), 2 m canopy air temperature (ΔT_{air}), and indoor air temperature (ΔT_b) between the TRAF and CNTL simulations. (a) June-July-August (JJA) mean at FR-Capitole. (b) December-January-February (DJF) mean at UK-Manchester. (c) and (b) JJA and DJF mean at UK-Manchester, respectively. The right y-axis indicates the normalized traffic heat flux, ranging from 0 to 1. Texts on the top are the daily mean ΔT_{grd}, ΔT_{air}, and ΔT_b, respectively. The right y-axis indicates the difference (Δ) between TRAF and CNTL simulations.

Traffic diurnal cycles (e.g., rush-hour peaks) directly influence the diurnal variations in ΔT_{grd}. In contrast, ΔT_{air} exhibited a delayed response and was less strongly affected. ΔT_b exhibits smaller diurnal variations than both ΔT_{grd} and ΔT_{air}. During summer mornings at FR-Capitole, difference in T_{grd} between TRAF and CNTL simulations (ΔT_{grd}) and ΔT_{air} increased in parallel with the normalized $Q_{traffic}$ (Figure 12(a)). After the morning traffic peak subsided, both ΔT_{grd} and ΔT_{air} declined moderately. The day-night difference in ΔT_{air} was minimal, with summer daytime ΔT_{air} of 0.29°C at 15:00 and nighttime ΔT_{air} of 0.25°C at 03:00, a difference of only a 0.04°C (Figure 13(a), (b)). The UK-Manchester site exhibited more pronounced diurnal variations in ΔT_{air}, where summer daytime ΔT_{air} of 0.07 at 15:00 and nighttime ΔT_{air} of 0.27 at 03:00 resulting

in a contrast of 0.2°C, primarily driven by the evening traffic peak (Figure 14(a), (b)). During the morning, ΔT_{air} at UK-Manchester decreased as heat accumulated overnight was gradually released.

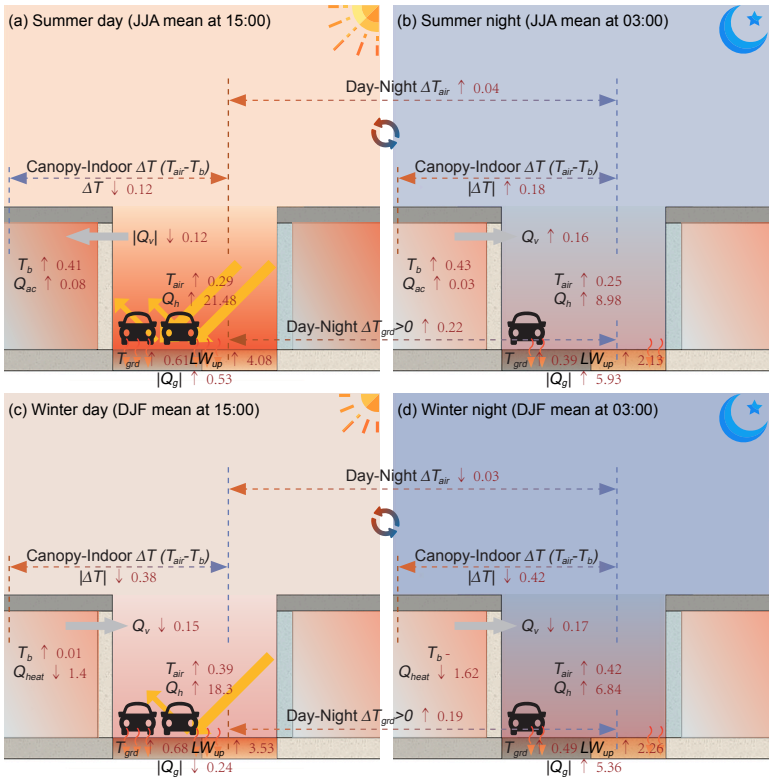

Figure 13. Traffic-induced changes in heat flux and temperatures at the FR-Capitole site in summer and winter, shown for 15:00 and 03:00 local time. The values represent differences between the TRAF and CNTL simulations. Red upward/downward arrows indicate increasing or decreasing trends, respectively. Q_{ac} is air-conditioning heat flux. LW_{up} is upward longwave radiation. Q_{g} is the heat flux into the ground. Q_{v} is ventilation heat flux. Q_{heat} is building space heating flux. T_{air} is canopy air temperature. T_{grd} is ground temperature. T_{b} is indoor temperature. | | denotes the absolute magnitude of negative values.

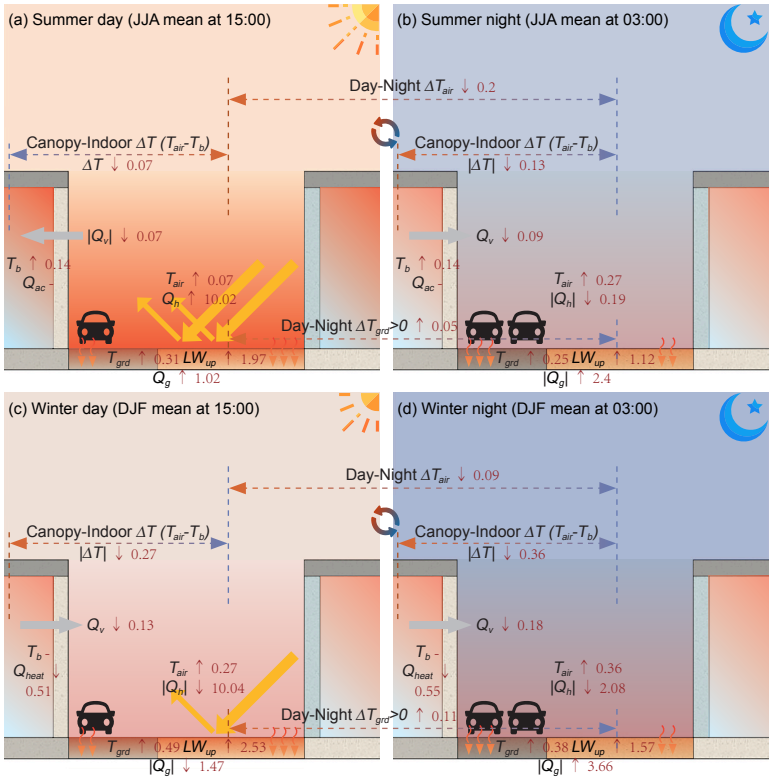

Figure 14. Traffic-induced changes in heat flux and temperatures at the UK-Manchester site in summer and winter, shown for 15:00 and 03:00 local time. The values represent differences between the TRAF and CNTL simulations. Red upward/downward arrows indicate increasing or decreasing trends, respectively. Q_{ac} is air-conditioning heat flux. LW_{up} is upward longwave radiation. Q_{g} is the heat flux into the ground. Q_{v} is ventilation heat flux. Q_{heat} is building space heating flux. T_{air} is canopy air temperature. T_{grd} is ground temperature. T_{b} is indoor temperature. | | denotes the absolute magnitude of negative values.

In addition to urban form and traffic timing, seasonal variations also influence the diurnal patterns and intensity of traffic-induced temperature changes, reflecting differences in background climate and building energy use conditions. Given located in temperate climate zones, both sites displayed a bimodal pattern in wintertime ΔT_{grd} and ΔT_{air}, with peaks occurring around 10:00 and 23:00 (Figure 12(b), (d)). At UK-Manchester, diurnal mean ΔT_{air} reached 0.35°C in winter, twice the counterpart of 0.17°C in summer. Warmer air within the urban canyon contributed to reduced snow depth on urban surfaces, potentially affecting the timing and intensity of urban road de-icing operations. Differences in T_{b} between TRAF and CNTL simulations (ΔT_{b}) were close to 0°C at both sites, as CLMU's building energy model activated urban space heating to maintain T_{b} above the minimum threshold. The diurnal variation patterns of ΔT_{b} may differ in urban areas within tropical climates, where air conditioning is more dominant in regulating indoor temperature.

4.4 Seasonal Variations in Model Sensitivity to Traffic Heat Flux

At the FR-Capitole site, Q_{h} and Q_{le} were sensitive to traffic perturbations (Figure 15(a)). In summer, σ of Q_{le} varied from 0.53 (−80% AADT) to 0.61 (+80% AADT) and σ of Q_{le} varied from 1.06 (−80% AADT) to 1.11 (+80% AADT). This suggested

that adding traffic heat flux provided more turbulent heat flux available to be partitioned into sensible and latent heat flux. σ lower than 1 indicates that despite increasing AADT by 80%, the simulated Q_{h} variation was still lower than observations. Comparatively, LW_{up} and Q_{tau} showed limited sensitivity to changes in Q_{traffic}, with a normalized standard deviation (σ) of 1.49 $\pm$ 0.006 and 0.53 $\pm$ 0.003 in summer, respectively. Flux variables were generally more sensitive to traffic heat in winter when radiation was not as strong as in summer. Traffic heat became an ignorable source of wintertime Q_{h}, whose σ varied from 0.49 to 0.62.

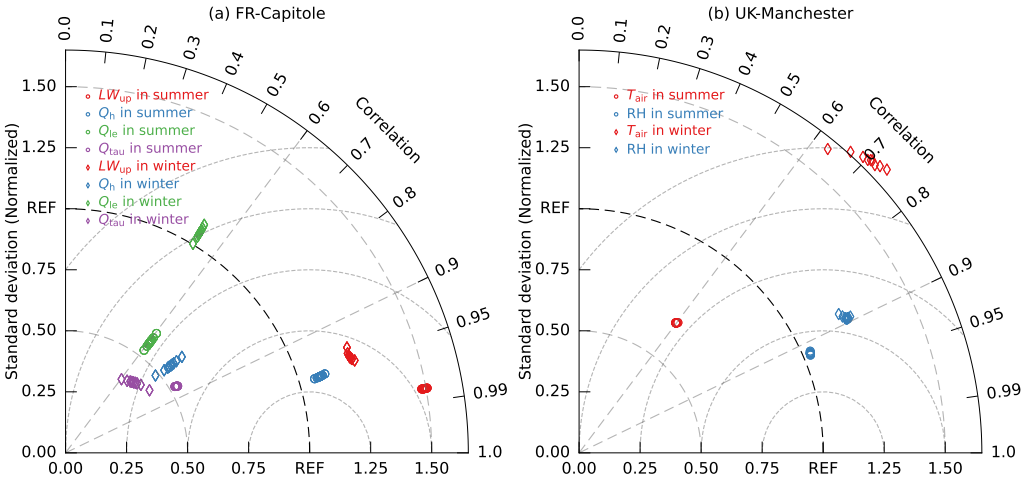

Figure 15. Taylor diagrams for June-July-August (summer) mean and December-January-February (winter) mean variables. (a) Upward longwave radiation (LW_{up}), sensible heat flux (Q_{h}), latent heat flux (Q_{le}), and momentum flux (Q_{tau}) at the FR-Capitole site. (b) Near-surface air temperature (T_{air}) and relative humidity (RH) at the UK-Manchester site. Symbols denote results from TRAF simulations in which perturbation factors of ±10%, ±20%, ±40%, and ±80% were applied to annual average daily traffic volume. "REF" denotes the reference dataset from observation. The radial distance between the origin and the symbols represents the normalized standard deviation σ. σ close to 1 is better. The azimuthal position indicates the correlation between modeled data and observed data, with correlation coefficient ρ denoted by the intersection between the radial line and the circle axis. ρ close to 1 is better. The contours centered on "REF" on the horizontal axis represent *E'*, the normalized centered root-mean square difference. *E'* close to 0 is better.

Simulations at the UK-Manchester site showed that both T_{air} and RH were insensitive to Q_{traffic} variations in summer (Figure 15(b)). Mean T_{air} varied from 21.33°C (−80% AADT) to 21.56 °C (+80% AADT), lower than the observed mean T_{air} of 21.83°C during 16 to 23 July 2022. Warming effects were more obvious in winter, when increasing AADT by 80% showed higher T_{air} by 0.3°C than decreasing AADT by 80%. Winter also showed more variations in σ and ρ of RH than summer. As RH in winter is higher than in summer, more air moisture is likely to be influenced by traffic heat perturbation. It should be noted that our simulations focused on model sensitivity under temperate climate conditions, where traffic heat emerged as a notable additional energy source. Different climate zones may exhibit distinct responses.

5 Conclusion

This study introduces a traffic module into the Community Earth System Model (CESM) for modeling traffic heat flux in urban areas. The method for estimating traffic heat was chosen after carefully considering multiple factors (i.e, spatial resolution, model complexity, computational cost) and making trade-offs to balance model detail and computational efficiency within the Earth system modeling framework. In the context of the urban surface energy balance, a variable representing traffic heat flux is added at the canyon floor, where the energy is subsequently redistributed, first warming the ground, then the canopy air, and finally the indoor air. The module was validated by conducting control (CNTL) and traffic (TRAF) simulations at the Capitole of Toulouse, France (FR-Capitole), and Manchester, UK (UK-Manchester) sites with measured data.

At the FR-Capitole site, incorporating an annual mean Q_{traffic} of 22.23 W/m^2 in 2004 increased the simulated annual averages of sensible heat flux (Q_{h}) by 15.78 W/m^2. RMSE of monthly mean Q_{h} between the TRAF simulation and observation was reduced to 17.0 W/m^2, lower than RMSE in the CNTL simulation of 29.6 W/m^2. At the UK-Manchester site, an annual mean Q_{traffic} of 16.27 W/m^2 in 2022 also produced better air temperature (T_{air}) and relative humidity. It increased T_{air} by 0.16°C in summer, whereas by 0.35°C in winter. Traffic-induced warming influenced not only temperature but also moisture, contributing to variations in human heat stress metrics. It increased the 2 m US National Weather Service Heat Index (NWS_HI), a temperature-driven metric, causing it to exceed the critical threshold of danger (40°C) by a cumulative 1.9°C·hours during the July 2022 heatwave at UK-Manchester. However, the 2 m Simplified Wet-Bulb Globe Temperature (sWBGT) and 2 m Discomfort Index (DI) occasionally decreased due to reduced humidity associated with traffic-induced drying.

Despite similar annual average daily traffic volume at FR-Capitole and UK-Manchester, the resulting thermal impacts varied. During summer, daytime T_{air} at 15:00 increased by 0.29°C at FR-Capitole, compared to only 0.07°C at UK-Manchester. This difference is attributed to denser building configurations, a narrower canyon, and less pervious road surfaces at FR-Capitole. Nighttime T_{air} at 03:00 increased by 0.25°C at FR-Capitole, comparable to the 0.27°C rise simulated at UK-Manchester. Due to a roof fraction and canyon height-to-width ratio at FR-Capitole nearly twice those of UK-Manchester, indoor temperature increases were more pronounced—0.42°C during summer nighttime at FR-Capitole versus 0.14°C at UK-Manchester. The lower building density at UK-Manchester facilitated greater heat dissipation, mitigating indoor warming. Overall, traffic-induced thermal effects are stronger in densely built environments where heat becomes trapped within the canyon and buildings. The diurnal traffic profile also plays a role, with higher evening traffic volumes likely contributing to prolonged nighttime warming, particularly during summer. Sensitivity analysis further showed that models were more sensitive to traffic perturbations in winter than in summer. Given that both FR-Capitole and UK-Manchester were located in the template climate zone, the urban environment has limited downward energy in winter, where traffic sensible heat becomes a non-ignorable heat source.

Future work will involve validating the model across more sites that represent diverse traffic conditions, background climate, and urban surface characteristics to assess its performance and traffic-induced thermal impacts. This will involve developing a global dataset of annual average daily traffic volume and vehicle types to support global simulations using CESM with the new traffic module. The simulated AHF at each model timestep preserves realistic short-term variability, capturing diurnal and event-driven fluctuations. Monthly and yearly mean values can then be evaluated with existing global AHF datasets (e.g., Dong et al., 2017; K. Jin et al., 2019; A. C. G. Varquez et al., 2021; Yang et al., 2017). Such intercomparisons between simulated and inventory-based AHF estimation will help assess uncertainties introduced by the building energy model and the new traffic module. Furthermore, global and regional simulations in coupled mode will allow investigation of atmospheric feedback to AHF. The new module, which includes

vehicle type classification, also enables future urban climate projections under energy transition scenarios, such as the shift from internal combustion engine vehicles to electric vehicles.

Appendix A Abbreviation and Acronyms

Table A1. Environmental Variable Definition.

Variable name	Long name	Unit	Source
AHF	Anthropogenic heat flux	W/m^2	Equation 3
Canopy-Indoor ΔT	Difference between T_{air} and T_b	°C	T_{air} minus T_b
Day-Night ΔT_{air}	Difference in T_{air} between day and night	°C	T_{air} at 15:00 minus T_{air} at 03:00
Day-Night ΔT_{grd}	Difference in T_{grd} between day and night	°C	T_{air} at 15:00 minus T_{air} at 03:00
DI	2 m discomfort index	°C	CTSM output
LW_{down}	Downward longwave radiation	W/m^2	CTSM output
LW_{up}	Upward longwave radiation	W/m^2	CTSM output
NWS_HI	2 m US National Weather Service Heat Index	°C	CTSM output
Q_{ac}	Air conditioning flux	W/m^2	CTSM output
Q_g	Heat flux into the ground	W/m^2	CTSM output
Q_h	Sensible heat flux	W/m^2	CTSM output
Q_{heat}	Building space heating flux	W/m^2	CTSM output
Q_{le}	Latent heat flux	W/m^2	CTSM output
Q_{tau}	Momentum flux	kg/m s^2	CTSM output
$Q_{traffic}$	Traffic heat flux	W/m^2	CTSM output
Q_v	Building ventilation flux	W/m^2	CTSM output
Q_w	Building waste heat flux	W/m^2	CTSM output
RH	2 m relative humidity	%	CTSM output
R_n	Net radiation flux	W/m^2	Equation 2
sWBGT	2 m simplified Wet-Bulb Globe Temperature	°C	CTSM output
SW_{down}	Downward solar radiation	W/m^2	CTSM output
SW_{up}	Upward solar radiation	W/m^2	CTSM output
T_{air}	2 m air temperature	°C	CTSM output
T_b	Building indoor temperature	°C	CTSM output
T_{grd}	Ground temperature	°C	CTSM output
ΔT_{air}	Difference in 2 m air temperature between TRAF and CNTL simulation	°C	T_{air} from TRAF minus T_{air} from CNTL
ΔT_b	Difference in indoor air temperature between TRAF and CNTL simulation	°C	T_b from TRAF minus T_b from CNTL
ΔT_{grd}	Difference in ground temperature between TRAF and CNTL simulation	°C	T_{grd} from TRAF minus T_{grd} from CNTL

Appendix B Community Terrestrial Systems Model (CTSM)

B1 Community Land Model Urban (CLMU)

CTSM's land component takes a sub-grid approach to represent land surface, where urban areas are classified into three types: tall building district (TBD), high density (HD), and medium density (MD) (Figure B1(a)). Each class of urban landunit consists of five surface types: roof, sunlit wall, shade wall, pervious road, and impervious road. The CLMU is a single-layer urban canopy model, driven by atmospheric forcing at a certain reference height (Figure B1(b)). CLMU has a building energy model, whose building space heating and waste heat sensible heat flux is moved to the canyon floor (i.e., pervious road and impervious road) (Figure B1(c)). Traffic-related sensible heat flux is added only to the canyon floor rather than to the canopy air (Figure B1(d)). We acknowledge that it is not consistent with real-world conditions, as heat from the exhaust and cooling systems was emitted directly into the air. However, due to the model configuration, we decided to add it to the floor and partition it into impervious and pervious roads.

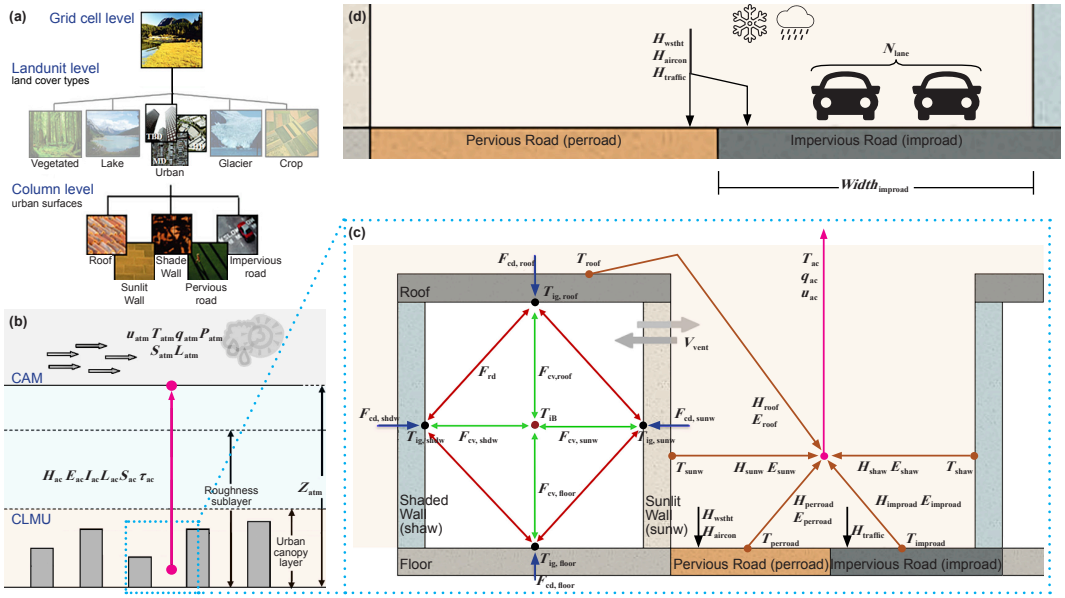

Figure B1. Community Land Model (CLM). (a) CLM representation hierarchy. (b) Interaction between the Community Atmosphere Model (CAM) and Community Land Model Urban (CLMU). (c) Parameterization of CLMU. (d) Urban traffic modeling. Subplot (a)–(c) were modified based on Y. Sun et al. (2024).

Appendix C Urban Traffic Heat Flux Estimation

Sailor and Lu (2004)'s top-down method of quantifying traffic heat flux (Q_{traffic}) is (Equation C1):

$$Q_{\text{traffic}}(t) = \text{pcDVD} \cdot \text{EneV} \cdot F_t \cdot pop_t, \tag{C1}$$

where pcDVD is per capita Daily Vehicle Distance (km/person day), F_t is hourly fractional traffic profile (%), pop_t is the hourly population density (person/km^2), and EneV is energy release per vehicle per meter (J/m).

Smith et al. (2009)'s more bottom-up method is (Equation C2):

$$Q_{\text{traffic}} = \frac{N_{\text{m,r}} \cdot \frac{L_r}{S_r} \cdot EF_{m,r} \cdot \lambda_m}{A}, \tag{C2}$$

where m indexes vehicle types, r indexes road, $N_{\text{m,r}}$ is the number of vehicles of type m on road r, L_r is the road length (m), S_r is the vehicle speed (m/s), $EF_{m,r}$ is the emission function per vehicle and road (g/km), λ_m is the net heat generated of fuel combustion (KJ/g) and A is the impact area (m^2).

Our newly developed urban traffic model adopted the bottom-up method, involving both constant and time-varying parameters (Table C1).

Table C1. List of Traffic Parameters.

Parameter name	Unit	Long name	Attribute	Reference & Data source
N_{lane}	Unitless	Number of vehicle lanes	Varying by urban classes and locations	Model default surface data and Equation 5
$Width_{\text{improad}}$	m	Impervious road width	Varying by urban classes and locations	Model default surface data and Equation 6
Speed	m/s	Fundamental vehicle speed	Simplified as a constant (40 m/s)	Pigeon et al. (2008); World Health Organization (2018)
E_{vehicle}	kW	Fundamental heat release into climate system per vehicle	Varying by vehicle types	Gasoline: Prusa et al. (2002); Diesel: Lee et al. (2017); Electric vehicle (EV): Ivanchev et al. (2020)
AADT	vehicles/day-lane	Annual average daily traffic volume	Varying by urban classes, locations, and years	Loder et al. (2019)
p_v	Unitless (0–1)	Fraction of vehicle types	Varying by vehicle types, locations and years	European Automotive Manufacturers Association (2024); International Energy Agency (IEA) (2024)

Based on Equation 5 and 6, we calculated global maps of the number of vehicle lanes (N_{lane}) using CTSM's default land surface dataset. N_{lane} is highest in TBD areas, with a maximum of six lanes in North America (Figure C1(a)). In contrast, some regions in Africa and South Asia do not have vehicle lanes, as the impervious road width is smaller than 1.75 m (Figure C1(b), (c)).

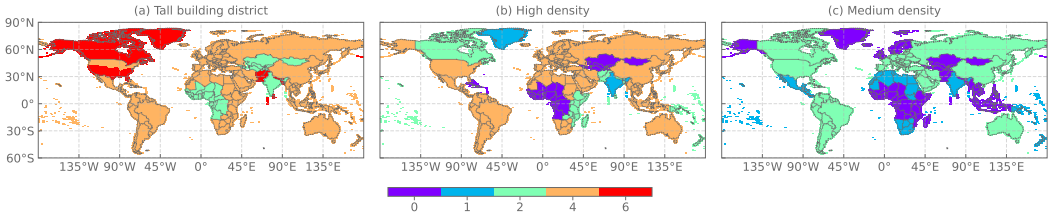

Figure C1. Number of vehicle lanes (N_{lane}) for CLMU's default urban classes: (a) Tall building district, (b) High density, and (c) Medium density.

Appendix D Simulations

D1 Input Data

CLMU represents FR-Capitole and UK-Manchester with morphological, radiative, and thermal parameters (Table D1).

Table D1. Urban Parameters.

Parameter name	Long name	Unit	FR-Capitole	UK-Manchester
CANYON_HWR	Canyon height-to-width ratio	Unitless	1.32	0.75
HT_ROOF	Height of roof	meter	15	26
NLEV_IMPROAD	Number of impervious road layers	Unitless	2	
THICK_ROOF	Thickness of roof	meter	0.14	0.15
THICK_WALL	Thickness of wall	meter	0.29	
WIND_HGT_CANYON	Height of wind in canyon	meter	7.5	13
WTLUNIT_ROOF	Fraction of roof	Unitless	0.62	0.35
WTROAD_PERV	Fraction of pervious road out of total canyon floor	Unitless	0.26	0.69
ALB_IMPROAD_DIF/ ALB_IMPROAD_DIR	Diffuse/direct albedo of impervious road	Unitless	0.13	
ALB_PERROAD_DIF/ ALB_PERROAD_DIR	Diffuse/direct albedo of pervious road	Unitless	0.13	0.08
ALB_ROOF_DIF/ ALB_ROOF_DIR	Diffuse/direct albedo of roof	Unitless	0.18	0.23
ALB_WALL_DIF/ ALB_WALL_DIR	Diffuse/direct albedo of wall	Unitless	0.23	0.27
EM_IMPROAD	Emissivity of impervious road	Unitless	0.97	0.91
EM_PERROAD	Emissivity of pervious road	Unitless	0.99	0.94
EM_ROOF	Emissivity of roof	Unitless	0.92	0.89
CV_IMPROAD	Volumetric heat capacity of impervious road	KJ m^{-3} K^{-1}	[2060.5, 1712.3, 0, 0, 0, 0, 0, 0, 0, 0]	
CV_ROOF	Volumetric heat capacity of roof	KJ m^{-3} K^{-1}	[1957.2, 994, 994, 1.2, 1.2, 1.2, 10.08, 10.08, 10.08, 609]	[1700, 1.2, 994, 1.2, 1.2, 1.2, 10.08, 10.08, 10.08, 609]
CV_WALL	Volumetric heat capacity of wall	KJ m^{-3} K^{-1}	[1524, 1525, 166, 918, 772, 771, 772, 227, 204, 628]	[1521, 1521, 138, 919, 773, 773, 773, 226, 194, 621]
TK_IMPROAD	Thermal conductivity of impervious road	W m^{-1} K^{-1}	[1.67, 0.56, 0, 0, 0, 0, 0, 0, 0, 0]	
TK_ROOF	Thermal conductivity of roof	W m^{-1} K^{-1}	[1.15, 0.15, 0.15, 0.03, 0.03, 0.03, 0.04, 0.04, 0.04, 0.16]	[1.2, 0.03, 0.15, 0.03, 0.03, 0.03, 0.04, 0.04, 0.04, 0.16]
TK_WALL	Thermal conductivity of wall	W m^{-1} K^{-1}	[2.03, 6.15, 5.85, 6.21, 4.77, 0.66, 4.77, 5.7, 5.85, 1.81]	[2.52, 2.52, 0.15, 2.11, 0.68, 0.68, 0.68, 1.6, 2.23, 2.3]

1 At FR-Capitole, urban parameters are from Urban-PLUMBER's detailed experiment. Among them, emissivity parameters are derived from CLM5.0's default dataset. That is, EM_IMPROAD, EM_PERROAD, and EM_ROOF were 0.97, 0.99, and 0.92, respectively. In the new dataset used for the CTSM development version, these values have been updated to 0.91, 0.95, and 0.91.

D2 Human Heat Stress Index

CLM has a module "HumanIndexMod" to quantify human heat stress indicators (Buzan et al., 2015), through which we selected three indicators: 2 m US National Weather Service Heat Index (NWS_HI), 2 m Simplified Wet-Bulb Globe Temperature (sWBGT), and 2 m Discomfort Index (DI). NWS_HI is calculated (Equation D1):

$$\begin{aligned}\mathrm{NWS\_HI} = &-42.379 + 2.04901523 \times T_\mathrm{f} + 10.14333127 \times \mathrm{RH} - 0.22475541 \times T_\mathrm{f} \times \mathrm{RH} \\ &- 6.83783 \times 10^{-3} \times T_\mathrm{f}^2 - 5.481717 \times 10^{-2} \times \mathrm{RH}^2 \\ &+ 1.22874 \times 10^{-3} \times T_\mathrm{f}^2 \times \mathrm{RH} \\ &+ 8.5282 \times 10^{-4} \times T_\mathrm{f} \times \mathrm{RH}^2 - 1.99 \times 10^{-6} \times T_\mathrm{f}^2 \times \mathrm{RH}^2,\end{aligned} \tag{D1}$$

where T_f is the air temperature in Fahrenheit (°F), RH is the relative humidity (%). sWBGT is calculated as (Equation D2):

$$\mathrm{sWBGT} = 0.567 \times T_\mathrm{c} + 0.393 \times \frac{V_\mathrm{p}}{100} + 3.94, \tag{D2}$$

where T_c is the air temperature (°C), V_p is the vapour pressure (Pa). DI is calculated as (Equation D3):

$$\mathrm{DI} = 0.5 \times T_\mathrm{w} + 0.5 \times T_\mathrm{c}, \tag{D3}$$

where T_w is the 2 m wet-bulb temperature (°C).

D3 Anthropogenic heat flux

Table D2. List of Annual Mean Anthropogenic Heat Flux (AHF, unit: W/m^2).

Site name	FR-Capitole	UK-Manchester
CNTL simulation	6.45 for 2004	9.99 for 2022
TRAF simulation	27.91 for 2004	25.86 for 2022
AH4GUC for the 2010s (A. C. G. Varquez et al., 2021)	41.78	21.4
K. Jin et al. (2019)'s global gridded dataset for 2015	19.6	29.9
AH-DMSP for 2010 (Yang et al., 2017)	0.1	0.6

D4 Taylor Diagram Metrics

The normalized standard deviation (σ) between modeled data and observation is calculated as (Equation D4):

$$\sigma = \sqrt{\sum_{t=1}^{T} \frac{(y_t - \bar{y})^2}{(x_t - \bar{x})^2}}, \tag{D4}$$

where $\bar{y}$ and $\bar{x}$ are the means of y_t and x_t, respectively. The correlation coefficient (ρ) is calculated by (Equation D5):

$$\rho = \frac{\sum_{t=1}^{T}(x_t - \bar{x}) \cdot (y_t - \bar{y})}{\sqrt{\sum_{t=1}^{n}(x_t - \bar{x})^2 \cdot \sum_{t=1}^{n}(x_t (y_t - \bar{y})^2}}, \tag{D5}$$

and the centered root-mean-square difference (E') is calculated as (Equation D6):

$$E' = \sqrt{\frac{1}{T} \cdot \sum_{t=1}^{T} [(y_t - \bar{y}) - (x_t - \bar{x})]^2}. \tag{D6}$$

In the Taylor diagrams, σ, ρ, and E' are interrelated by (Equation D7):

$$E' = \sqrt{{\sigma_y}^2 + {\sigma_x}^2 - 2 \cdot \sigma_y \cdot \sigma_x \cdot \rho} = \sqrt{{\sigma_x}^2 \cdot (\frac{{\sigma_y}^2}{{\sigma_x}^2} + 1 - 2 \cdot \frac{\sigma_y}{\sigma_x} \cdot \rho)} = \sqrt{\sigma^2 + 1 - 2 \cdot \sigma \cdot \rho}, \tag{D7}$$

when considering that the σ_x of observation dataset is 1.

Open Research

Community Earth System Model (CESM) source code is open access: `https://github.com/ESCOMP/CESM`. Community Terrestrial Systems Model (CTSM) source code is available at: `https://github.com/ESCOMP/CTSM` (CTSM Development Team, 2024b). The CTSM default input data set is available at `https://svn-ccsm-inputdata.cgd.ucar.edu/trunk/inputdata/lnd/clm2`. Urban-PLUMBER data is open access at (M. Lipson et al., 2021). Sensor data is open access at (Y. Sun, Bannan, et al., 2025). Global 1 km anthropogenic heat flux data, AH4GUC, is available at (A. C. Varquez et al., 2020). The modified code, simulation input, scripts for data analysis, and other supplementary materials are available in the author's GitHub repository (Y. Sun & Zheng, 2025).

Acknowledgments

This work was supported by the Natural Environment Research Council [grant number UKRI1294], and the UKRI Harmonised Impact Acceleration Account, funded via the Economic & Social Research Council [grant number ES/X004759/1] and Engineering & Physical Sciences Research Council [grant number EP/X525753/1]. This work used the ARCHER2 UK National Supercomputing Service (`https://www.archer2.ac.uk`) and JASMIN, the UK's collaborative data analysis environment (`https://www.jasmin.ac.uk`). We gratefully acknowledge the data from Transport for Greater Manchester (TfGM)'s VivaCity video analytics sensors. We appreciate Dr. Xiaodan Xu from Lawrence Berkeley National Laboratory for her valuable insights. Z.Z. appreciates the support provided by the academic start-up funds from the Department of Earth and Environmental Sciences at The University of Manchester. Y.S. is supported by Z.Z.'s academic start-up funds. Contributions from K.W.O. are based upon work supported by the NSF National Center for Atmospheric Research, which is a major facility sponsored by the U.S. National Science Foundation under Cooperative Agreement No. 1852977. The authors declare no conflict of interest.

References

Afshari, A., Schuch, F., & Marpu, P. (2018). Estimation of the traffic related anthropogenic heat release using BTEX measurements – A case study in Abu Dhabi. *Urban Climate*, *24*, 311–325. doi: 10.1016/j.uclim.2017.02.001

Ayartürk, H., Doruk, E., Durgun, İ., & Ekbiç, K. (2016). New Heating System Development Working with Waste Heat for Electric Vehicles. *Transportation Research Procedia*, *14*, 1080–1086. doi: 10.1016/j.trpro.2016.05.178

Beck, H. E., McVicar, T. R., Vergopolan, N., Berg, A., Lutsko, N. J., Dufour, A., ... Miralles, D. G. (2023). High-resolution (1 km) Köppen-Geiger maps for 1901–2099 based on constrained CMIP6 projections. *Scientific Data*, *10*(1), 724. doi: 10.1038/s41597-023-02549-6

Billot, R., El Faouzi, N.-E., & De Vuyst, F. (2009). Multilevel Assessment of the Impact of Rain on Drivers' Behavior: Standardized Methodology and Empirical Analysis. *Transportation Research Record*, *2107*(1), 134–142. doi: 10.3141/2107-14

Block, A., Keuler, K., & Schaller, E. (2004). Impacts of anthropogenic heat on regional climate patterns. *Geophysical Research Letters*, *31*(12). doi: 10.1029/2004GL019852

Bohnenstengel, S. I., Hamilton, I., Davies, M., & Belcher, S. E. (2014). Impact of anthropogenic heat emissions on London's temperatures. *Quarterly Journal of the Royal Meteorological Society*, *140*(679), 687–698. doi: 10.1002/qj.2144

Bueno, B., Norford, L., Pigeon, G., & Britter, R. (2011). Combining a Detailed Building Energy Model with a Physically-Based Urban Canopy Model. *Boundary-Layer Meteorology*, *140*(3), 471–489. doi: 10.1007/s10546-011-9620-6

Bueno, B., Pigeon, G., Norford, L. K., Zibouche, K., & Marchadier, C. (2012). Development and evaluation of a building energy model integrated in the TEB scheme. *Geoscientific Model Development*, *5*(2), 433–448. doi: 10.5194/gmd-5-433-2012

Buzan, J. R., Oleson, K. W., & Huber, M. (2015). Implementation and comparison of a suite of heat stress metrics within the Community Land Model version 4.5. *Geoscientific Model Development*, *8*(2), 151–170. doi: 10.5194/gmd-8-151-2015

Chapman, L., & Thornes, J. E. (2005). The influence of traffic on road surface temperatures: Implications for thermal mapping studies. *Meteorological Applications*, *12*(4), 371–380. doi: 10.1017/S1350482705001957

Chen, B., Dong, L., Shi, G., Li, L.-J., & Chen, L.-F. (2014). Anthropogenic Heat Release: Estimation of Global Distribution and Possible Climate Effect. *Journal of the Meteorological Society of Japan. Ser. II*, *92A*, 157–165. doi: 10.2151/jmsj.2014-A10

Chen, F., Kusaka, H., Bornstein, R., Ching, J., Grimmond, C. S. B., Grossman-Clarke, S., ... Zhang, C. (2011). The integrated WRF/urban modelling system: Development, evaluation, and applications to urban environmental problems. *International Journal of Climatology*, *31*(2), 273–288. doi: 10.1002/joc.2158

Chen, F., Yang, X., & Wu, J. (2016). Simulation of the urban climate in a Chinese megacity with spatially heterogeneous anthropogenic heat data. *Journal of Geophysical Research: Atmospheres*, *121*(10), 5193–5212. doi: 10.1002/2015JD024642

Cheng, Y., Zhao, L., Chakraborty, T. C., Oleson, K., Demuzere, M., Liu, X., ... Li, X. C. (2025). U-Surf: A global 1 km spatially continuous urban surface property dataset for kilometer-scale urban-resolving Earth system modeling. *Earth System Science Data*, *17*(5), 2147–2174. doi: 10.5194/essd-17-2147-2025

Chow, W. T. L., Salamanca, F., Georgescu, M., Mahalov, A., Milne, J. M., & Ruddell, B. L. (2014). A multi-method and multi-scale approach for estimating city-wide anthropogenic heat fluxes. *Atmospheric Environment*, *99*, 64–76. doi: 10.1016/j.atmosenv.2014.09.053

CTSM Development Team. (2024a). ESCOMP/CTSM: Add LILAC (ctsm1.0.dev104) [Software]. *Zenodo*. doi: 10.5281/zenodo.11176758

CTSM Development Team. (2024b). ESCOMP/CTSM: ctsm5.2.005: Fix clm6_0 defaults and CESM testing issues, add tests to detect these problems (ctsm5.2.005) [Software]. *Zenodo*. doi: 10.5281/zenodo.13324334

Demuzere, M., Kittner, J., Martilli, A., Mills, G., Moede, C., Stewart, I. D., ... Bechtel, B. (2022). A global map of local climate zones to support earth system modelling and urban-scale environmental science. *Earth System Science Data*, *14*(8), 3835–3873. doi: 10.5194/essd-14-3835-2022

Dong, Y., Varquez, A. C. G., & Kanda, M. (2017). Global anthropogenic heat flux database with high spatial resolution. *Scientific Data*, *150*, 276–294. doi: 10.1016/j.atmosenv.2016.11.040

Donkers, A., Yang, D., & Viktorović, M. (2020). Influence of driving style, infrastructure, weather and traffic on electric vehicle performance. *Transportation Research Part D: Transport and Environment*, *88*, 102569. doi: 10.1016/j.trd.2020.102569

European Automotive Manufacturers Association. (2021). *Vehicles in use, Europe 2021* (Tech. Rep.). European Automobile Manufacturers' Association (ACEA).

European Automotive Manufacturers Association. (2024). *Vehicles on European Roads 2024* (Tech. Rep.). European Automotive Manufacturers Association.

Ferreira, M. J., de Oliveira, A. P., & Soares, J. (2011). Anthropogenic heat in the city of São Paulo, Brazil. *Theoretical and Applied Climatology*, *104*(1), 43–56. doi: 10.1007/s00704-010-0322-7

Fischer, E. M., Oleson, K. W., & Lawrence, D. M. (2012). Contrasting urban and rural heat stress responses to climate change. *Geophysical Research Letters*, *39*(3), L0370. doi: 10.1029/2011GL050576

Flanner, M. G. (2009). Integrating anthropogenic heat flux with global climate models. *Geophysical Research Letters*, *36*(2), L02801. doi: 10.1029/2008GL036465

Fujimoto, A., Saida, A., & Fukuhara, T. (2012). A New Approach to Modeling Vehicle-Induced Heat and Its Thermal Effects on Road Surface Temperature. *Journal of Applied Meteorology and Climatology*(11), 1980-1993. doi: 10.1175/JAMC-D-11-0156.1

Goret, M., Masson, V., Schoetter, R., & Moine, M.-P. (2019). Inclusion of CO2 flux modelling in an urban canopy layer model and an evaluation over an old European city centre. *Atmospheric Environment: X*, *3*, 100042. doi: 10.1016/j.aeaoa.2019.100042

Haklay, M., & Weber, P. (2008). OpenStreetMap: User-Generated Street Maps. *IEEE Pervasive Computing*, *7*(4), 12–18. doi: 10.1109/MPRV.2008.80

Hertwig, D., Ng, M., Grimmond, S., Vidale, P. L., & McGuire, P. C. (2021). High-resolution global climate simulations: Representation of cities. *International Journal of Climatology*, *41*(5), 3266–3285. doi: 10.1002/joc.7018

Husni, E., Prayoga, G. A., Tamba, J. D., Retnowati, Y., Fauzandi, F. I., Yusuf, R., & Yahya, B. N. (2022). Microclimate investigation of vehicular traffic on the urban heat island through IoT-Based device. *Heliyon*, *8*(11), e11739. doi: 10.1016/j.heliyon.2022.e11739

Iamarino, M., Beevers, S., & Grimmond, C. S. B. (2012). High-resolution (space, time) anthropogenic heat emissions: London 1970–2025. *International Journal of Climatology*, *32*(11), 1754–1767. doi: 10.1002/joc.2390

International Energy Agency (IEA). (2024). *Global EV Outlook 2024* (Tech. Rep.). Paris: International Energy Agency (IEA). Retrieved from `https://www.iea.org/reports/global-ev-outlook-2024`

Ivanchev, J., Fonseca, J., & Knoll, A. (2020). Electrification and Automation of Road Transport: Impact Analysis of Heat and Carbon Emissions for Singapore. In *2020 IEEE 23rd International Conference on Intelligent Transportation Systems (ITSC)* (pp. 1–8). doi: 10.1109/ITSC45102.2020.9294274

Jägerbrand, A. K., & Sjöbergh, J. (2016). Effects of weather conditions, light conditions, and road lighting on vehicle speed. *SpringerPlus*, *5*(1), 505. doi: 10.1186/s40064-016-2124-6

Jin, K., Wang, F., Chen, D., Liu, H., Ding, W., & Shi, S. (2019). A new global gridded anthropogenic heat flux dataset with high spatial resolution and long-term time series. *Scientific Data*, *6*(1), 139. doi: 10.1038/s41597-019-0143-1

Jin, L., Xu, X., Wang, Y., Lazar, A., Sadabadi, K. F., Spurlock, C. A., ... Asudegi, M. (2024). Macroscopic Traffic Modeling Using Probe Vehicle Data: A Ma-

chine Learning Approach. *Data Science for Transportation*, *6*(3), 17. doi: 10.1007/s42421-024-00102-4

Juruš, P., Resler, J., Derbek, P., Krč, P., Belda, M., Benešová, N., ... Hrubeš, P. (2016). High resolution modelling of anthropogenic heat from traffic in urban canopy: A sensitivity study. In *2016 Smart Cities Symposium Prague (SCSP)* (pp. 1–6). doi: 10.1109/SCSP.2016.7501031

Khalifa, A., Bouzouidja, R., Marchetti, M., Buès, M., Bouilloud, L., Martin, E., & Chancibaut, K. (2018). Individual contributions of anthropogenic physical processes associated to urban traffic in improving the road surface temperature forecast using TEB model. *Urban Climate*, *24*, 778–795. doi: 10.1016/j.uclim.2017.09.003

Khalifa, A., Marchetti, M., Bouilloud, L., Martin, E., Bues, M., & Chancibaut, K. (2016). Accounting for anthropic energy flux of traffic in winter urban road surface temperature simulations with the TEB model. *Geoscientific Model Development*, *9*(2), 547–565. doi: 10.5194/gmd-9-547-2016

Kikegawa, Y., Tanaka, A., Ohashi, Y., Ihara, T., & Shigeta, Y. (2014). Observed and simulated sensitivities of summertime urban surface air temperatures to anthropogenic heat in downtown areas of two Japanese Major Cities, Tokyo and Osaka. *Theoretical and Applied Climatology*, *117*(1), 175–193. doi: 10.1007/s00704-013-0996-8

Kim, Y., Yeo, H., & Kim, Y. (2022). Estimating urban spatial temperatures considering anthropogenic heat release factors focusing on the mobility characteristics. *Sustainable Cities and Society*, *85*, 104073. doi: 10.1016/j.scs.2022.104073

Lee, J., Chu, S., Min, K., Kim, M., Jung, H., Kim, H., & Chi, Y. (2017). Classification of diesel and gasoline dual-fuel combustion modes by the analysis of heat release rate shapes in a compression ignition engine. *Fuel*, *209*, 587–597. doi: 10.1016/j.fuel.2017.07.067

Li, X. C., Zhao, L., Oleson, K., Zhou, Y., Qin, Y., Zhang, K., & Fang, B. (2024). Enhancing urban climate-energy modeling in the Community Earth System Model (CESM) through explicit representation of urban air-conditioning adoption. *Journal of Advances in Modeling Earth Systems*, *16*(4), e2023MS004107. doi: 10.1029/2023MS004107

Li, X. C., Zhao, L., Qin, Y., Oleson, K., & Zhang, Y. (2024). Elevated urban energy risks due to climate-driven biophysical feedbacks. *Nature Climate Change*, *14*(10), 1056–1063. doi: 10.1038/s41558-024-02108-w

Lipson, M., Grimmond, S., Best, M., Christen, A., Coutts, A., Crawford, B., ... Kim, Y.-H. (2021). Urban-PLUMBER: Site information webpage (archive of https://urban-plumber.github.io/sites) (2021-09-20) [Dataset]. *Zenodo*. doi: 10.5281/zenodo.4751557

Lipson, M. J., Grimmond, S., Best, M., Abramowitz, G., Coutts, A., Tapper, N., ... Pitman, A. J. (2023). Evaluation of 30 urban land surface models in the Urban-PLUMBER project: Phase 1 results. *Quarterly Journal of the Royal Meteorological Society*, *150*(758), 126-169. doi: 10.1002/qj.4589

Liu, B., Xie, Z., Qin, P., Liu, S., Li, R., Wang, L., ... Shi, C. (2021). Increases in Anthropogenic Heat Release from Energy Consumption Lead to More Frequent Extreme Heat Events in Urban Cities. *Advances in Atmospheric Sciences*, *38*(3), 430–445. doi: 10.1007/s00376-020-0139-y

Liu, C., S., Yusak O., & and Karlström, A. (2017). Weather variability and travel behaviour – what we know and what we do not know. *Transport Reviews*, *37*(6), 715–741. doi: 10.1080/01441647.2017.1293188

Loder, A., Ambühl, L., Menendez, M., & Axhausen, K. W. (2019). Understanding traffic capacity of urban networks. *Scientific Reports*, *9*(1), 16283. doi: 10.1038/s41598-019-51539-5

Manchester city council. (2022). *Manchester Electric Vehicle Charging Strategy*

(Tech. Rep.). Manchester: Manchester city council. Retrieved from `https://democracy.manchester.gov.uk/documents/s41761/EV%20Update.pdf`

Masson, V., Gomes, L., Pigeon, G., Liousse, C., Pont, V., Lagouarde, J.-P., ... Tulet, P. (2008). The Canopy and Aerosol Particles Interactions in TOulouse Urban Layer (CAPITOUL) experiment. *Meteorology and Atmospheric Physics*, *102*(3), 135–157. doi: 10.1007/s00703-008-0289-4

McCarthy, M. P., Best, M. J., & Betts, R. A. (2010). Climate change in cities due to global warming and urban effects. *Geophysical Research Letters*, *37*(9), L09705. doi: 10.1029/2010GL042845

McCarthy, M. P., Harpham, C., Goodess, C. M., Jones, P. D., Xian, G., Shi, H., ... Kolian, M. (2012). Simulating climate change in UK cities using a regional climate model, HadRM3. *GIScience & Remote Sensing*, *32*(12), 1875–1888. doi: 10.1002/joc.2402

Met Office. (n.d.). *What Is a Heatwave?* (Retrieved August 2, 2025, from https://www.metoffice.gov.uk/weather/learn-about/weather/types-of-weather/temperature/heatwave)

Ming, Y., Liu, Y., & Liu, X. (2022). Spatial pattern of anthropogenic heat flux in monocentric and polycentric cities: The case of Chengdu and Chongqing. *Sustainable Cities and Society*, *78*, 103628. doi: 10.1016/j.scs.2021.103628

Mužić, I., Hodnebrog, Ø., Yilmaz, Y. A., Berntsen, T. K., Lawrence, D. M., & Sobhani, N. (2025). The Evaluation of Hydroclimatic Variables Over Nordic Fennoscandia Using WRF-CTSM. *Journal of Geophysical Research: Atmospheres*, *130*(9), e2024JD043103. doi: 10.1029/2024JD043103

Neog, R., Acharjee, S., & Hazarika, J. (2021). Spatiotemporal analysis of road surface temperature (RST) and building wall temperature (BWT) and its relation to the traffic volume at Jorhat urban environment, India. *Environment, Development and Sustainability*, *23*(7), 10080–10092. doi: 10.1007/s10668-020-01047-8

Ohashi, Y., Genchi, Y., Kondo, H., Kikegawa, Y., Yoshikado, H., & Hirano, Y. (2007). Influence of Air-Conditioning Waste Heat on Air Temperature in Tokyo during Summer: Numerical Experiments Using an Urban Canopy Model Coupled with a Building Energy Model. *Journal of Applied Meteorology and climatology*, *46*, 66–81. doi: 10.1175/JAM2441.1

Oke, T. R., Mills, G., Christen, A., & Voogt, J. A. (2017). *Urban Climates*. Cambridge University Press.

Oleson, K. W., Bonan, G. B., Feddema, J. J., Vertenstein, M., & Kluzek, E. (2010). *Technical description of an urban parameterization for the Community Land Model (CLMU)* (Tech. Rep.). University Corporation for Atmospheric Research.

Oleson, K. W., & Feddema, J. (2020). Parameterization and surface data improvements and new capabilities for the Community Land Model Urban (CLMU). *Journal of Advances in Modeling Earth Systems*, *12*(2), e2018MS001586. doi: 10.1029/2018MS001586

Padget, E. D., Knapp, K. K., & Thomas, G. B. (2001). Investigation of Winter-Weather Speed Variability in Sport Utility Vehicles, Pickup Trucks, and Passenger Cars. *Transportation Research Record*, *1779*(1), 116–124. doi: 10.3141/1779-16

Pesaresi, M., & Politis, P. (2022). *GHS-BUILT-H R2022A - GHS building height, derived from AW3D30, SRTM30, and Sentinel2 composite (2018) - OBSOLETE RELEASE.* European Commission, Joint Research Centre (JRC). doi: 10.2905/CE7C0310-9D5E-4AEB-B99E-4755F6062557

Pigeon, G., Legain, D., Durand, P., & Masson, V. (2007). Anthropogenic heat release in an old European agglomeration (Toulouse, France). *International Journal of Climatology*, *27*(14), 1969–1981. doi: 10.1002/joc.1530

Pigeon, G., Moscicki, M. A., Voogt, J. A., & Masson, V. (2008). Simulation of

fall and winter surface energy balance over a dense urban area using the TEB scheme. *Meteorology and Atmospheric Physics*, *102*(3), 159–171. doi: 10.1007/s00703-008-0320-9

Prusa, J. M., Segal, M., Temeyer, B. R., Gallus, W. A., & Takle, E. S. (2002). Conceptual and Scaling Evaluation of Vehicle Traffic Thermal Effects on Snow/Ice-Covered Roads. *Journal of Applied Meteorology and Climatology*, *41*(12), 1225-1240. doi: 10.1175/1520-0450(2002)041⟨1225:CASEOV⟩2.0.CO;2

Rakha, H., Arafeh, M., & Park, S. (2012). Modeling Inclement Weather Impacts on Traffic Stream Behavior. *International Journal of Transportation Science and Technology*, *1*(1), 25–47. doi: 10.1260/2046-0430.1.1.25

Resler, J., Krč, P., Belda, M., Juruš, P., Benešová, N., Lopata, J., ... Kanani-Sühring, F. (2017). PALM-USM v1.0: A new urban surface model integrated into the PALM large-eddy simulation model. *Geoscientific Model Development*, *10*(10), 3635–3659. doi: 10.5194/gmd-10-3635-2017

Ryu, Y.-H., & Min, S.-K. (2024). Anthropogenic warming degrades spring air quality in Northeast Asia by enhancing atmospheric stability and transboundary transport. *npj Climate and Atmospheric Science*, *7*(1), 1–10. doi: 10.1038/s41612-024-00603-7

Sailor, D. J., Georgescu, M., Milne, J. M., & Hart, M. A. (2015). Development of a national anthropogenic heating database with an extrapolation for international cities. *Atmospheric Environment*, *118*, 7–18. doi: 10.1016/j.atmosenv.2015.07.016

Sailor, D. J., & Lu, L. (2004). A top–down methodology for developing diurnal and seasonal anthropogenic heating profiles for urban areas. *Atmospheric Environment*, *38*(17), 2737–2748. doi: 10.1016/j.atmosenv.2004.01.034

Shahmohamadi, P., Che-Ani, A. I., Maulud, K. N. A., Tawil, N. M., & Abdullah, N. a. G. (2011). The Impact of Anthropogenic Heat on Formation of Urban Heat Island and Energy Consumption Balance. *Urban Studies Research*, *2011*(1), 497524. doi: 10.1155/2011/497524

Skuza, A., & Jurecki, R. S. (2022). Analysis of factors affecting the energy consumption of an EV vehicle - a literature study. *IOP Conference Series: Materials Science and Engineering*, *1247*(1), 012001. doi: 10.1088/1757-899X/1247/1/012001

Smith, C., Lindley, S., & Levermore, G. (2009). Estimating spatial and temporal patterns of urban anthropogenic heat fluxes for UK cities: The case of Manchester. *Theoretical and Applied Climatology*, *98*(1), 19–35. doi: 10.1007/s00704-008-0086-5

Sun, R., Wang, Y., & Chen, L. (2018). A distributed model for quantifying temporal-spatial patterns of anthropogenic heat based on energy consumption. *Journal of Cleaner Production*, *170*, 601–609. doi: 10.1016/j.jclepro.2017.09.153

Sun, Y., Bannan, T. J., Topping, D. O., & Zheng, Z. (2025). Bias-corrected urban air temperature and relative humidity (Hourly, 2022-2024) in Greater Manchester (v1) [Dataset]. *figshare*. doi: 10.6084/m9.figshare.29828651.v1

Sun, Y., Fang, B., Oleson, K. W., Zhao, L., Topping, D. O., Schultz, D. M., & Zheng, Z. (2024). Improving urban climate adaptation modelling in the Community Earth System Model (CESM) through transient urban surface albedo representation. *Journal of Advances in Modeling Earth Systems*, *16*, e2024MS004380. doi: 10.1029/2024MS004380

Sun, Y., Oleson, K. W., Zhao, L., Mills, G., He, C., Demuzere, M., ... Zheng, Z. (2025). *Enhancing Global-scale Urban Land Cover Representation Using Local Climate Zones in the Community Earth System Model.* EarthArXiv. doi: 10.31223/X5GX4K

Sun, Y., & Zheng, Z. (2025). envdes/code_CLMU_traffic: First release (v0.0.0) [Software]. *Zenodo*. doi: 10.5281/zenodo.16886810

Takane, Y., Nakajima, K., & Kikegawa, Y. (2022). Urban climate changes during the COVID-19 pandemic: Integration of urban-building-energy model with social big data. *npj Climate and Atmospheric Science*, *5*(1), 1–10. doi: 10.1038/s41612-022-00268-0

Tanimura, R., Hiromori, A., Umedu, T., Yamaguchi, H., & Higashino, T. (2015). Prediction of Deceleration Amount of Vehicle Speed in Snowy Urban Roads Using Weather Information and Traffic Data. In *2015 IEEE 18th International Conference on Intelligent Transportation Systems* (pp. 2268–2273). doi: 10.1109/ITSC.2015.366

Tao, H., Xing, J., Pan, G., Pleim, J., Ran, L., Wang, S., ... Li, J. (2021). Impact of anthropogenic heat emissions on meteorological parameters and air quality in Beijing using a high-resolution model simulation. *Frontiers of Environmental Science & Engineering*, *16*(4), 44. doi: 10.1007/s11783-021-1478-3

Taylor, K. E. (2001). Summarizing multiple aspects of model performance in a single diagram. *Journal of Geophysical Research: Atmospheres*, *106*(D7), 7183–7192. doi: 10.1029/2000JD900719

Teufel, B., Sushama, L., Poitras, V., Dukhan, T., Bélair, S., Miranda-Moreno, L., ... Bitsuamlak, G. (2021). Impact of COVID-19-Related Traffic Slowdown on Urban Heat Characteristics. *Atmosphere*, *12*(2), 243. doi: 10.3390/atmos12020243

Varquez, A. C., Shota, K., Khanh, D. N., & Kanda, M. (2020). Global 1-km Present and Future Hourly Anthropogenic Heat Flux (v6) [Dataset]. *figshare*. doi: 10.6084/m9.figshare.12612458.v6

Varquez, A. C. G., Kiyomoto, S., Khanh, D. N., & Kanda, M. (2021). Global 1-km present and future hourly anthropogenic heat flux. *Scientific Data*, *8*(1), 64. doi: 10.1038/s41597-021-00850-w

Washington, W. M. (1972). Numerical Climatic-Change Experiments : The Effect of Man's Production of Thermal Energy. *Journal of Applied Meteorology (1962-1982)*, *11*(5), 768–772.

World Health Organization. (2018). *Global Status Report on Road Safety 2018* (Tech. Rep.). Geneva: World Health Organization.

Xiao, S., Neti, S., Suleiman, M. T., & Naito, C. (2018). A Modeling Approach of Heat Transfer of Bridges Considering Vehicle-Induced Thermal Effects. *Journal of Applied Meteorology and Climatology*, *57*(12), 2851–2869. doi: 10.1175/JAMC-D-17-0315.1

Xie, M., Liao, J., Wang, T., Zhu, K., Zhuang, B., Han, Y., ... Li, S. (2016). Modeling of the anthropogenic heat flux and its effect on regional meteorology and air quality over the Yangtze River Delta region, China. *Atmospheric Chemistry and Physics*, *16*(10), 6071–6089. doi: 10.5194/acp-16-6071-2016

Xie, Y., Li, Y., Zhao, Z., Dong, H., Wang, S., Liu, J., ... Duan, X. (2020). Microsimulation of electric vehicle energy consumption and driving range. *Applied Energy*, *267*, 115081. doi: 10.1016/j.apenergy.2020.115081

Yang, W., Luan, Y., Liu, X., Yu, X., Miao, L., & Cui, X. (2017). A new global anthropogenic heat estimation based on high-resolution nighttime light data. *Scientific Data*, *4*(1), 170116. doi: 10.1038/sdata.2017.116

Yu, J., Sun, Y., Lindley, S., Jay, C., Topping, D. O., Oleson, K. W., & Zheng, Z. (2025). Integration and execution of Community Land Model Urban (CLMU) in a containerized environment. *Environmental Modelling & Software*, *188*, 106391. doi: 10.1016/j.envsoft.2025.106391

Zhang, G. J., Cai, M., & Hu, A. (2013). Energy consumption and the unexplained winter warming over northern Asia and North America. *Nature Climate Change*, *3*(5), 466–470. doi: 10.1038/nclimate1803

Zhang, N., Wang, X., Chen, Y., Dai, W., & Wang, X. (2010). Numerical simulations on influence of urban land cover expansion and anthropogenic heat release on urban meteorological environment in Pearl River Delta. *Build-*

ing Services Engineering Research and Technology, *126*(3-4), 398–403. doi: 10.1007/s00704-015-1601-0

Zhao, L., Oleson, K., Bou-Zeid, E., Krayenhoff, E. S., Bray, A., Zhu, Q., ... Oppenheimer, M. (2021). Global multi-model projections of local urban climates. *Nature Climate Change*, *11*(2), 152–157. doi: 10.1038/s41558-020-00958-8

Zheng, Z., Zhao, L., & Oleson, K. W. (2021). Large model structural uncertainty in global projections of urban heat waves. *Nature Communications*, *12*(1), 3736. doi: 10.1038/s41467-021-24113-9